

---

## National Laser Users' Facility and External Users' Programs

During FY02, 698 target shots were taken on OMEGA for external users' experiments. This is the highest number of target shots ever taken by external users on OMEGA in a single year and represents a 16% increase in external user shots over FY01. The external user shots accounted for 49% of the total OMEGA target shots in FY02. External users' experiments were carried out by eight collaborative teams under the National Laser Users' Facility (NLUF) Program as well as collaborations led by scientists from Lawrence Livermore National Laboratory (LLNL), Los Alamos National Laboratory (LANL), Sandia National Laboratory (SNL), the Nuclear Weapons Effects Testing (NWET) Program, and the Commissariat à l'Énergie Atomique (CEA) of France.

### NLUF Programs

FY02 was the second of a two-year period of performance for the eight NLUF programs approved for FY01–FY02 experiments. The eight NLUF campaigns received a total of 118 target shots on OMEGA in FY02.

The Department of Energy (DOE) issued solicitations in mid-FY02 for NLUF proposals to be carried out in FY03–FY04. DOE raised the NLUF funding allocation to \$800,000 for FY03 and is expected to increase it to \$1,000,000 for FY04 to accommodate the high level of interest shown in the use of OMEGA to carry out experiments of relevance to the National Nuclear Security Agency (NNSA) Stockpile Stewardship Program. NLUF participants use these funds to cover their costs for carrying out experiments on OMEGA. The participants do not pay the OMEGA operating costs for carrying out their experiments; the operation of OMEGA is funded by the DOE-LLE Cooperative Agreement.

A total of 13 NLUF proposals were submitted to DOE for consideration for FY03–FY04 support and OMEGA shot allocation. An independent DOE Technical Evaluation Panel comprised of Dr. Tina Back (LLNL), Dr. David Bradley (LLNL), Dr. David Montgomery (LANL), and Dr. Richard Olson (SNL) reviewed the proposals on 10 June 2002 and recommended that up to nine of the proposals be approved for partial funding

and shot allocation during FY03–FY04. Table 92.VI lists the successful proposals.

### FY02 NLUF Experiments

The eight NLUF experiments carried out in FY02 included the following:

#### *Atomic Physics of Hot, Ultradense Plasmas.*

Principal Investigators: C. F. Hooper, Jr. (University of Florida), D. A. Haynes (Fusion Technology Institute, University of Wisconsin), and collaborators from Los Alamos National Laboratory, the University of Wisconsin, and LLE.

The objective of this study is to produce hot (electron temperature  $T_e > 1.5$  keV), dense (electron density  $\sim 5 \times 10^{24}$  cm<sup>-3</sup>) plasmas on OMEGA and to study these plasmas using x-ray spectroscopy. The focus of the work over the last two years has been on studying direct-drive implosions of CH shells filled with deuterium doped with Ar. A total of 11 shots were taken this year, and the results are currently being analyzed.

#### *Determination of Temperatures and Density Gradients in Implosion Cores of OMEGA Targets.*

Principal Investigators: R. C. Mancini (University of Nevada, Reno), J. A. Koch (LLNL), and collaborators from Prism Computational Sciences, LLE, LLNL, and Howard University.

The goal of this project is the spectroscopic determination of 1-D temperature and density gradients in implosion cores produced in OMEGA indirect-drive implosion experiments. The method is based on a novel self-consistent analysis of data from simultaneous x-ray line spectra and x-ray monochromatic images. This represents a significant advance on previous efforts of x-ray spectroscopy of implosion cores that relied solely on the analysis of space-integrated spectra to extract spatially averaged temperature and density in the core.

Targets consisted of Ar-doped, D<sub>2</sub>-filled plastic shells placed inside Au hohlraums, and the targets were driven by 30 OMEGA UV beams. During FY02, the spectroscopic method

Table 92:VI: List of successful FY03–FY04 NLUF Proposals.

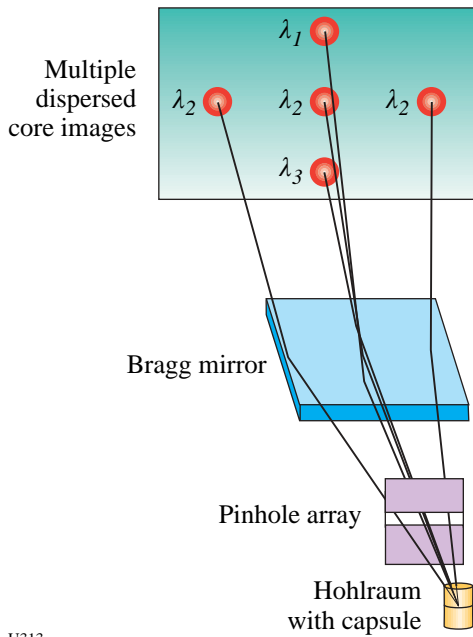
Principal Investigator	Affiliation	Proposal Title
R. P. Drake <i>et al.</i>	University of Michigan	Experimental Astrophysics on the OMEGA Laser
B. B. Afeyan	Polymath Research, Inc.	Optical Mixing Controlled Stimulated Scattering Instabilities: Generating Electron Plasma Waves and Ion-Acoustic Waves to Suppress Backscattering Instabilities
R. D. Petrasso and C. K. Li	Massachusetts Institute of Technology	Time Evolution of Capsule $\rho R$ and Proton Emission Imaging of Core Structure
C. McKee <i>et al.</i>	University of California, Berkeley	OMEGA Laser Studies of the Interaction of Supernova Blast Waves with Interstellar Clouds
R. K. Fisher	General Atomics	High-Spatial-Resolution Neutron Imaging of Inertial Fusion Target Plasmas Using Neutron Bubble Detectors
M. Meyers <i>et al.</i>	University of California, San Diego	Dynamic Properties of Shock-Compressed Single Crystals by <i>in-situ</i> Dynamic X-Ray Diffraction
H. Baldis <i>et al.</i>	University of California, Davis	Studies of Ion-Acoustic Waves (IAW) Under Direct-Drive NIF Conditions
R. Mancini <i>et al.</i>	University of Nevada, Reno	Experimental and Modeling Studies of 2-D Core Gradients in OMEGA Implosions
R. Jeanloz	University of California, Berkeley	Recreating Planetary Core Conditions on OMEGA

for core gradient determination was expanded in two ways. First, the original method based on the self-consistent analysis of Ar x-ray line spectra and Ar  $He_{\beta}$  line monochromatic images (i.e., two criteria) was extended to a three-criteria (i.e., more-stringent) method based on the search for plasma gradients that yield the best fits to x-ray line spectra and the Ar  $He_{\beta}$  and  $Ly_{\beta}$  monochromatic emissivities. The spatial distribution of monochromatic emissivities is extracted via an Abel inversion of intensity lineouts from x-ray images. This multi-objective data analysis problem is efficiently solved with a niched Pareto genetic algorithm. The algorithm is general and can be applied to other cases of multi-objective data analysis as well. Second, an alternative technique to analyze the temperature gradient was developed. It is based on the fact that the local ratio (i.e., point-by-point in the plasma source) of  $Ly_{\beta}$  to  $He_{\beta}$  emissivities is a strong function of the temperature with a weak (residual) dependence on the density. As a result, tem-

perature gradients can now be determined by two different techniques and cross-checked for consistency.

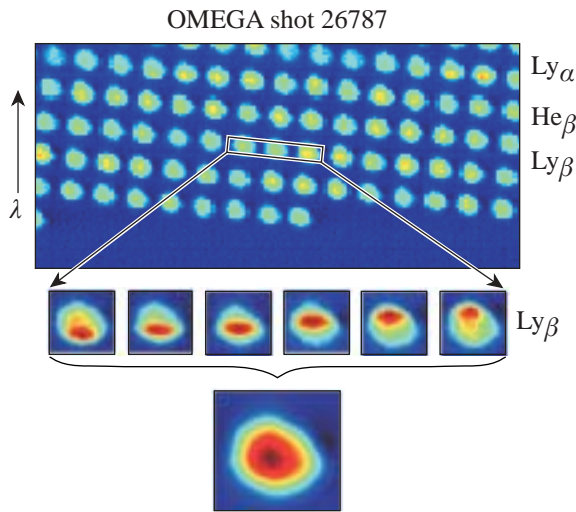
The MMI-2 x-ray imager for indirect-drive implosions was successfully fielded and tested. This new instrument uses a target-mounted pinhole array and a flat multilayer-mirror Bragg reflector to record numerous narrowband x-ray images spanning the 3- to 5-keV photon energy range (see Fig. 92.35). The pinhole diameters are 5  $\mu\text{m}$ , and the spatial resolution is 10  $\mu\text{m}$ .

Figure 92.36 shows typical data recorded by MMI-2. Each image spans  $\approx 75$  eV along the spectral axis. Groups of images can be combined to produce line-based images. Continuum-based images can also be extracted from the data. As a result, several line- and continuum-based images can now be recorded in the same shot. In particular, the problem of intensity



U313

Figure 92.35 Schematic illustrating the concept of the MMI-2 x-ray imager. A target-mounted pinhole array provides numerous high-resolution, high-brightness x-ray images, and in combination with a multilayer Bragg mirror, it produces an array of quasi-monochromatic dispersed core images. This multispectral imaging technique is based on an LLE-developed technique.<sup>1</sup>



U307

Figure 92.36 An array of implosion-core images recorded with MMI-2 in OMEGA shot 26787. Three Ar line transitions are indicated along the spectral dispersion axis:  $Ly_{\alpha}$  (3.734 Å),  $He_{\beta}$  (3.369 Å), and  $Ly_{\beta}$  (3.151 Å). The subgroup of six images shows different portions of each image covered by the  $Ly_{\beta}$  emission. This subgroup of images is used to produce the  $Ly_{\beta}$ -based image of the core shown at the bottom of the figure.

and structure of continuum-photon contribution to line-based images can now be addressed with greater accuracy. An interactive data language (IDL)-based code was written to process MMI-2 data, combine subgroups of images, and produce different types of x-ray core images.

*Studies of the Fundamental Properties of High-Energy Density Plasmas.*

Principal Investigator: R. D. Petrasso (MIT Plasma Science and Fusion Center) and collaborators from MIT, LLE, LLNL, and SUNY Geneseo.

Proper assembly of capsule mass in inertial confinement fusion (ICF) implosions is of fundamental importance for achieving ignition,<sup>2-4</sup> and experimental information about implosion dynamics is crucial both for understanding how assembly occurs and for validating numerical simulations. Without carefully tailored assembly of the fuel, hot-spot ignition planned for the National Ignition Facility (NIF)<sup>2-5</sup> and the Laser Megajoule Facility (LMJ)<sup>6</sup> will fail. Hot-spot ignition relies on shock coalescence to “ignite” the hot spot, followed by burn of the compressed “shell” material (compressive burn). The relationship between these events must be understood to ensure the success of ICF ignition.

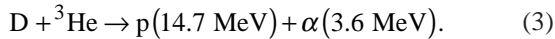
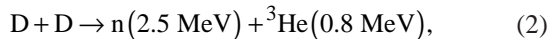
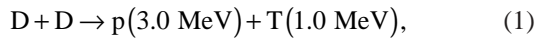
In the last year, the MIT/LLE collaboration, as part of the MIT NLUF program, obtained gated measurements of areal density ( $\rho R$ ) at pivotal moments in the target’s evolution: first at shock coalescence and then 400 ps later during compressive burn. These measurements were accomplished through the use of 14.7-MeV protons generated by the fusion of the fuel constituents—deuterium (D) and helium ( $^3\text{He}$ )—in imploding capsules with 24- $\mu\text{m}$ -thick plastic (CH) shells.<sup>7,8</sup> An accurate determination of  $\rho R$  evolution and asymmetry is made by measuring the proton energy downshift at different times and in many different directions.

Earlier measurements of  $\rho R$  utilizing primary 14.7-MeV protons<sup>7-9</sup> and secondary protons<sup>10</sup> concentrated on properties and dynamics during compressive burn for implosions of capsules with 20- $\mu\text{m}$ -thick CH shells. These studies included  $\rho R$  asymmetries,<sup>9-11</sup> fuel-shell mix,<sup>12-15</sup> and the effects of beam smoothing upon fuel  $\rho R$ .<sup>9,12,16</sup> In addition, x-ray absorption techniques<sup>17</sup> have been used to study aspects of  $\rho R$  modulations at peak compression and during decompression.

Direct-drive implosions were conducted on OMEGA, with 60 beams of frequency-tripled (351-nm) UV light in a 1-ns square pulse and a total energy of ~21 kJ.<sup>18</sup> Full smoothing of

the laser beams was used,<sup>12</sup> and beam-to-beam energy imbalance was typically  $\leq 5\%$  rms. Two types of hydrodynamically similar capsules were used, all with a nominal diameter of  $940\ \mu\text{m}$  and a shell thickness of  $24\ \mu\text{m}$ . CH-shell capsules were filled with approximately 6 atm of  $\text{D}_2$  and 12 atm of  $^3\text{He}$ . Capsules with shells of CD (or  $1\ \mu\text{m}$  of CD inside of  $23\ \mu\text{m}$  of CH) were filled with approximately 20 atm of  $^3\text{He}$ . The principal diagnostics for this work were high-resolution, charged-particle spectrometers simultaneously viewing each implosion from different directions (the spectrometers and their properties are described in Ref. 8). In addition, the neutron temporal diagnostic (NTD) measured the D fusion burn histories.<sup>19</sup>

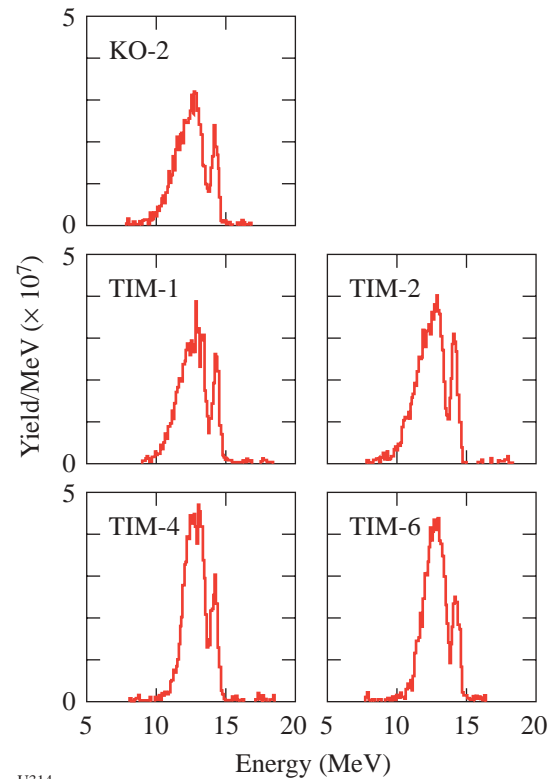
The following reactions occur in imploding capsules fueled with D and  $^3\text{He}$ :



This analysis uses the high-energy proton of Reaction (3) because it can easily penetrate the larger  $\rho R$  during compressive burn while, in contrast, the 3.0-MeV protons of Reaction (1) are ranged out. Figure 92.37 shows proton spectra obtained simultaneously at five different viewing angles for shot 24811. In each spectrum, two distinct peaks are clearly evident. The narrow, higher-energy peak is associated with burn of  $\sim 40$ -ps duration at shock coalescence, while the broader, lower-energy peak is associated with the  $\sim 150$ -ps compressive burn that occurs about 400 ps after the shock.<sup>20</sup> For each of the two peaks in each spectrum, the average energy downshift of the 14.7-MeV protons was evaluated and is shown in Fig. 92.38 along with data from several other shots. Through the use of plasma stopping power calculations,<sup>21</sup> these energy downshifts are related to the capsule  $\rho R$  (Fig. 92.38 and Table 92.VII). The capsule  $\rho R$  at shock coalescence, which occurs  $1.7 \pm 0.1$  ns after the beginning of the 1-ns laser pulse, is  $\sim 13.0 \pm 2.5\ \text{mg}/\text{cm}^2$ . During compressive burn, the average  $\rho R$  increases to  $70 \pm 8\ \text{mg}/\text{cm}^2$ . Since the temperature of the shell is at or below 1 keV at both shock and compression times, and since nearly all energy loss occurs through the shell,<sup>7,10</sup> these  $\rho R$  determinations are insensitive to exact values of the evolving temperature and density.<sup>21</sup> Table 92.VII summarizes the data of Fig. 92.38, which also show that asymmetries as large as  $30\ \text{mg}/\text{cm}^2$  in areal density

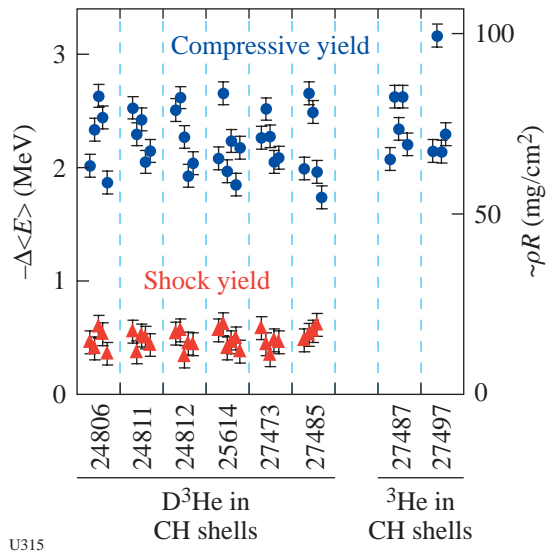
exist during compressive burn in these implosions. This effect has been reported for capsules with  $20\text{-}\mu\text{m}$ -thick shells<sup>9,10</sup> and for cryogenic capsules.<sup>10</sup>

The ion temperature at shock burn can be measured from the spectra. As shown in Fig. 92.39, the shock peak is well fit by a Gaussian. After accounting for the effects of the instrument response,<sup>7,8</sup> a Doppler-derived ion temperature of  $6 \pm 1$  keV is obtained. This temperature is higher than the neutron-derived Doppler-width temperature characterizing the compressive burn, which is about 3 keV. This method of temperature determination from the width of the 14.7-MeV proton spectrum has been previously used for thin-shell, high-temperature implosions.<sup>7</sup> At shock burn (for thick-shell implosions), the shell is relatively “thin,” the shock-induced ion temperature is relatively high, and the duration ( $\sim 40$  ps) is sufficiently short that little evolution in  $\rho R$  occurs. In contrast, the compression



U314

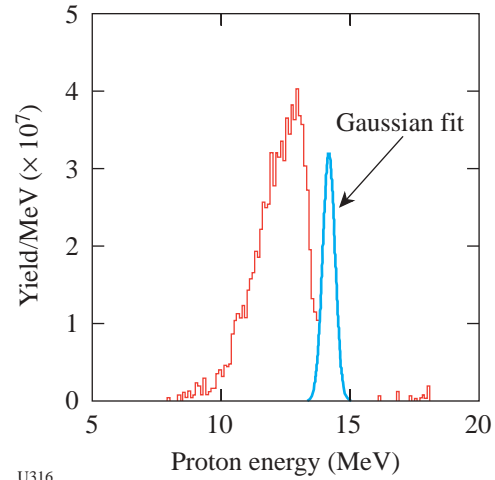
Figure 92.37  
Spectra of high-energy protons generated from the fusion of D and  $^3\text{He}$  in an imploding ICF capsule (shot 24811). The spectrometers viewed the implosion from five different directions; each plot is identified by the OMEGA port used.<sup>8</sup> The narrow high-energy peak is associated with shock-coalescence burn; the broad low-energy peak is associated with compressive burn.



U315

Figure 92.38

The average energy downshifts (from 14.7 MeV) for the shock and compression burn peaks of each spectrum from shot 24811 (as shown in Fig. 92.37) and from several others. From plasma stopping power calculations,<sup>21</sup> values of  $\langle\rho R\rangle$  can be associated with the plotted values of  $\Delta E_p$ , and the right-hand vertical axis scale is meant to show the approximate correspondence (Table 92.VII lists more-exact values for averages over groups of shots).



U316

Figure 92.39

A shock-induced ion temperature can be determined by fitting a Gaussian to the shock peak, correcting for the instrument response, and assuming Doppler broadening. For this spectrum the result is 6.8 keV, and the mean for all spectra from this shot (24811) is 6 keV with a standard deviation of 1 keV.

Table 92.VII: Values of  $\langle\rho R\rangle$  inferred from measured  $D^3He$  proton energy losses (calculated with the slowing-down formalism of Ref. 21, using energies averaged over all available spectra for each shot). For capsules with  $D^3He$  fuel and CH shells, it was assumed that the slowing was dominated by CH at  $T_e \leq 1$  keV and  $\rho = 2$  g/cm<sup>3</sup> at shock coalescence or 20 g/cm<sup>3</sup> at compression burn. For capsules with  $^3He$  fuel in CD shells, which produce no shock yield, it was assumed that the slowing was dominated by CD at  $T_e \leq 1$  keV and  $\rho = 20$  g/cm<sup>3</sup>. The “ $\pm$ ” refers not to measurement uncertainties but to the standard deviation about the mean of individual measurements for each shot.

Shot	Fuel	Shell	$\langle\rho R\rangle_{\text{shock}}$ (mg/cm <sup>2</sup> )	$\langle\rho R\rangle_{\text{comp}}$ (mg/cm <sup>2</sup> )
24086	18 atm D <sup>3</sup> He	24 $\mu\text{m}$ CH	13.2 $\pm$ 2.6	70.6 $\pm$ 9.7
24811	18 atm D <sup>3</sup> He	24 $\mu\text{m}$ CH	13.3 $\pm$ 2.0	71.6 $\pm$ 6.1
24812	18 atm D <sup>3</sup> He	24 $\mu\text{m}$ CH	13.0 $\pm$ 2.5	71.1 $\pm$ 9.2
25614	18 atm D <sup>3</sup> He	24 $\mu\text{m}$ CH	13.7 $\pm$ 2.6	67.6 $\pm$ 8.7
27473	18 atm D <sup>3</sup> He	24 $\mu\text{m}$ CH	12.9 $\pm$ 2.3	70.1 $\pm$ 5.8
27485	18 atm D <sup>3</sup> He	24 $\mu\text{m}$ CH	15.2 $\pm$ 1.6	67.8 $\pm$ 12.1
27474	20 atm <sup>3</sup> He	24 $\mu\text{m}$ CD	—	79.5 $\pm$ 8.3
27479	20 atm <sup>3</sup> He	24 $\mu\text{m}$ CD	—	81.5 $\pm$ 16.4

burn peak for the protons (as noted previously<sup>7</sup>) is far wider than the Doppler width and, the effects of measured asymmetry<sup>7-9</sup> and geometry<sup>8</sup> notwithstanding, largely reflects  $\rho R$  evolution over the compressive burn ( $\sim 150$  ps).

To validate the interpretation that the high-energy peak (Fig. 92.37) is due to shock coalescence, and to explore other important aspects of implosion physics, a second series of implosions were performed using a hydrodynamically similar capsule with 20 atm of  $^3\text{He}$  in a 24- $\mu\text{m}$ -thick CD shell. Spectra from these implosions [see the example in Fig. 92.40(b)] show a single compression peak downshifted in energy by about the same amount as measured in the first series of experiments [see Fig. 92.40(a)]. Notably absent, however, is the shock peak in Fig. 92.40(a) that occurs between 14 and 15 MeV. This means that no D from the shell has mixed into the central, high-temperature region at shock time.<sup>22</sup> Conversely, by the time of compressive burn, mixing of the CD shell with the  $^3\text{He}$  must have occurred (Fig. 92.40) in order for  $\text{D}^3\text{He}$  reactions to be present (see Refs. 12–15 for more discussion of mix).

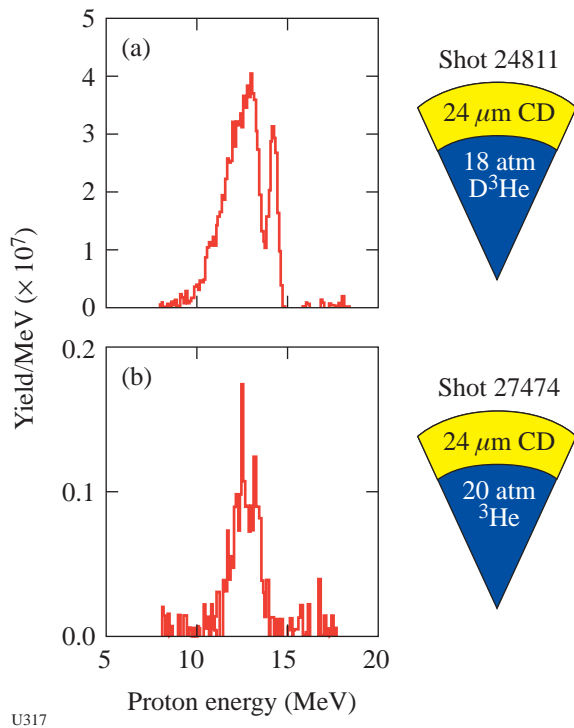


Figure 92.40 The shock-induced burn that is present in plot (a) is absent when the fuel is changed to pure  $^3\text{He}$  within a CD shell [plot (b)], although the compressive burn is still present because of fuel-shell mix. Besides validating the identification of the shock-induced peak, these data demonstrate the absence of fuel-shell mix in the central regions of the capsule at shock coalescence.

The spectrum of Fig. 92.40(b) can also be directly interpreted to mean that, at least for these implosions, the shell is not riddled with holes during compressive burn even though low-mode asymmetries exist (Fig. 92.38). If there were holes, there would be a high-energy peak in Fig. 92.40(b). This issue is important since concern exists as to whether shell breakup, as a consequence of Rayleigh–Taylor instability, occurs prior to burn propagation and ignition, thereby quenching ignition.

To improve the understanding of the physical processes and to test the validity of 1-D hydrodynamic simulations in realistic circumstances, we show a comparison of simulated<sup>23</sup> and experimental charged-particle spectra in Fig. 92.41. The basic structure of the experimental data is reproduced reasonably well by the simulation. Of particular relevance is the comparison at shock coalescence since, as experimentally demonstrated, the effects of mix are minimal and 1-D simulations should be at their most accurate because they do not include mix effects. In this context, the ratio of experimental yield to theoretical yield [so called yield-over-clean (YOC)] is about 60%; the predicted  $\rho R$  is 10  $\text{mg}/\text{cm}^2$  while the experimental value is 13  $\text{mg}/\text{cm}^2$ ; the predicted shock temperature is 8 keV, while the measurement is  $6 \pm 1$  keV. It is also noteworthy that the predicted interval between shock and compression burn is 500 ps, while the measured interval is  $\sim 400$  ps. Since shock timing and coalescence are critical to ignition at the NIF and the LMJ,<sup>2-6</sup> experiments to test the limits of validity of ignition simulation codes should be helpful to this endeavor. In addition, it seems entirely plausible that similar measurements could be made at the NIF at various phases in the development and testing of ignition capsules.

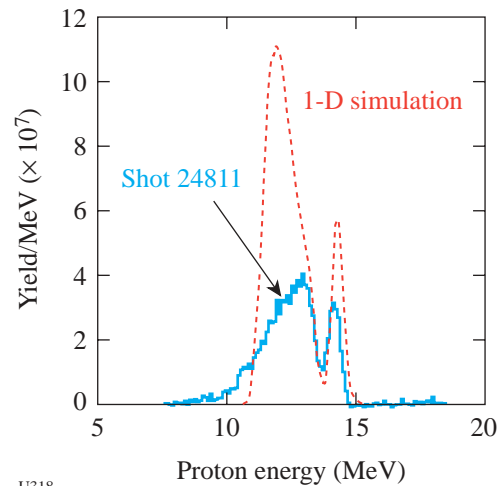


Figure 92.41 A comparison of 1-D simulation to data from shot 24811.

In summary, the first measurements of  $\rho R$  evolution occurring in ICF implosions were conducted in the course of this past year's work on this program. In the 400-ps interval between shock coalescence and compression burn, the azimuthally averaged  $\rho R$  changed from  $13.0 \pm 2.5$  to  $70 \pm 8$  mg/cm<sup>2</sup>. The experiments demonstrated that fuel-shell mix has not occurred in the central regions of the imploding capsule at shock coalescence, and that the shock-induced temperature is about 6 keV. As mix is inconsequential at this stage of the implosion, these and other measured parameters offer a sensitive test of 1-D shock physics simulations. The experiments further demonstrated that, at least for these types of implosions, gaps and holes do not riddle the shell at compression burn.

Several intriguing avenues exist for advancing these measurements and improving the understanding of implosion dynamics. As  $\rho R$  is sufficiently small at shock coalescence, 3.0-MeV protons from Reaction (1) will readily penetrate the shell and lead, in principle, to an even more accurate measurement of the shell  $\rho R$  at that instant. Such experiments, as well as higher-accuracy spectrometers for D<sup>3</sup>He fusion reactions, are being planned. With more-accurate  $\rho R$  measurements at shock coalescence, studies will be undertaken to establish whether  $\rho R$  asymmetries exist at that time, and whether these asymmetries persist and amplify through the compression burn phase,<sup>10,11</sup> thereby accounting for the notable asymmetries that have been measured at that critical stage.

*High-Spatial-Resolution Neutron Imaging of Inertial Fusion Target Plasmas Using Bubble Neutron Detectors.*

Principal Investigator: R. K. Fisher (General Atomics) and collaborators from LLE, CEA, and LLNL.

Bubble detectors that can detect neutrons with a spatial resolution of 5 to 30  $\mu\text{m}$  are a promising approach to high-resolution imaging of NIF target plasmas. Gel bubble detectors were used in successful proof-of-principle imaging experiments on OMEGA. The results were presented in an invited talk at the October 2001 Meeting of the Division of Plasma Physics of the American Physical Society and published in *Physics of Plasmas*.<sup>24</sup>

Until recently, bubble detectors appeared to be the only approach capable of achieving neutron images of NIF targets with the desired 5- $\mu\text{m}$  spatial resolution in the target plane. In 2001, however, NIF reduced the required standoff distance from the target, so that diagnostic components can now be placed as close as 10 cm to the target plasma. This will allow neutron imaging with higher magnification and may make it

possible to obtain 5- $\mu\text{m}$ -resolution images on the NIF using deuterated scintillators.

Since gel detectors (which consist of  $\sim 10$ - $\mu\text{m}$ -diam drops of bubble detector liquid suspended in an inactive support gel that occupies  $\sim 99\%$  of the detector volume) are easy to use, they were chosen for the initial tests on OMEGA. The bubbles could be photographed several hours after the neutron exposure. Imaging NIF target plasmas at neutron yields of  $10^{15}$  will require a higher-detection-efficiency detector. A liquid bubble chamber detector should result in an  $\sim 1000$ -times-higher neutron detection efficiency, which is comparable to that possible using scintillation detectors.

A pressure-cycled liquid bubble detector will require a light-scattering system to record the bubble locations a few microseconds after neutron exposure, when the bubbles have grown to be  $\sim 10$   $\mu\text{m}$  in diameter. The next major task planned under this grant will be to perform experimental tests to determine how accurately the spatial distribution of the bubble density can be measured under the conditions expected in the NIF. The bubble density will be large enough to produce significant overlap in the two-dimensional images, so we will need to be able to measure bubbles behind bubbles. One of the goals of these tests is to determine if a simple light-transmission approach is feasible. One of the concerns at very high bubble densities is that light scattered out of the path can be rescattered back into the transmitted light path by bubbles in neighboring paths.

*Examination of the "Cone-in-Shell" Target Compression Concept for Asymmetric Fast Ignition.\**

Principal Investigators: R. B. Stephens (General Atomics) and collaborators from LLNL and the Institute of Laser Engineering (ILE), Osaka University, Osaka, Japan.

Investigation of the compression hydrodynamics of fast-ignition targets continued in FY02 with several shots taken on "cone-in-shell" indirect-drive targets. The results from these experiments showed that while the hydrodynamic codes used to design these targets captured the gross dynamics well, there were details of the experiment that were not predicted by the code calculations.

---

\*This work was performed under the auspices of the U.S. Department of Energy under Contract No. DE-FG03-00SF2229, by the University of California, Lawrence Livermore National Laboratory under Contract No. W-7405-ENG-48, and with the additional corporate support of General Atomics.

The separation of compression and ignition in the fast-ignition (FI) concept<sup>25</sup> requires a new approach to target design. The strict symmetry and smoothness requirements of a target compressed to generate and enclose an ignition spark by dense, cold fuel are replaced by a much more complex set of considerations. The fusion burn is optimized by creation of a uniformly dense fuel mass. The symmetry of that mass is relatively unimportant, but its surface must be pure DT and accessible to an ignition beam. The ignition energy must be delivered by a short-pulse laser, but the compression drive can be accomplished by any means—laser (direct and indirect drive), heavy ion beam, or z-pinch.

S. Hatchett (LLNL) designed an indirect-drive target based on the cone-in-shell FI target concept<sup>26</sup> [Fig. 92.42(a)]: A hollow cone is inserted in the side of the shell to provide a protected line of sight to the assembled fuel mass. Modeling suggests that the presence of the cone substantially changes the target's implosion dynamics [Fig. 92.42(b)]; surprisingly, one should achieve the most-compact target with a deliberately

asymmetric drive [Fig. 92.42(c)]. The modeling might not properly capture details of the flow as the shell slides down along the cone surface; there is a concern that high-Z material from the cone might mix into the assembled fuel mass, thereby hindering ignition. This model was tested on a scale-1 hohlraum at OMEGA. Each collapse was radiographed with an x-ray framing camera, which took a sequence of 16 x-radiographs (Fig. 92.43). With this information it was possible to determine the implosion velocity and diameter, density, and symmetry at stagnation. X-ray images were taken alternately through different filters to identify any gold contamination in the assembled fuel. The experimental radiographs were very similar to the simulations; apparently the effect of the inserted cone was well described by *LASNEX* modeling, and both the shell and the drive were smooth enough that compression instabilities had minimal effect. As predicted, it was found that an asymmetric drive does seem to result in a more-compact target, but that that configuration also generates a gas flow that blows out the tip of the cone just about at the stagnation point. There were subtle differences between simulation and experiment.

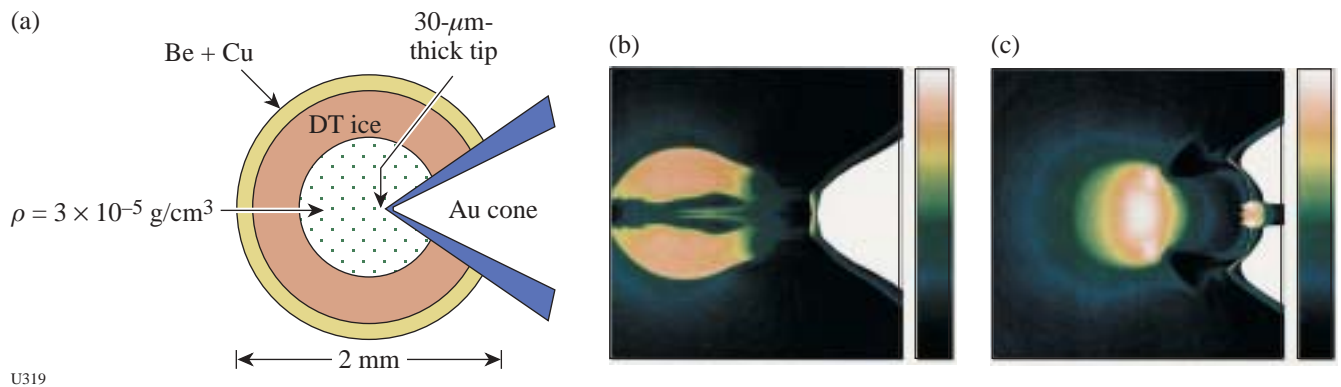
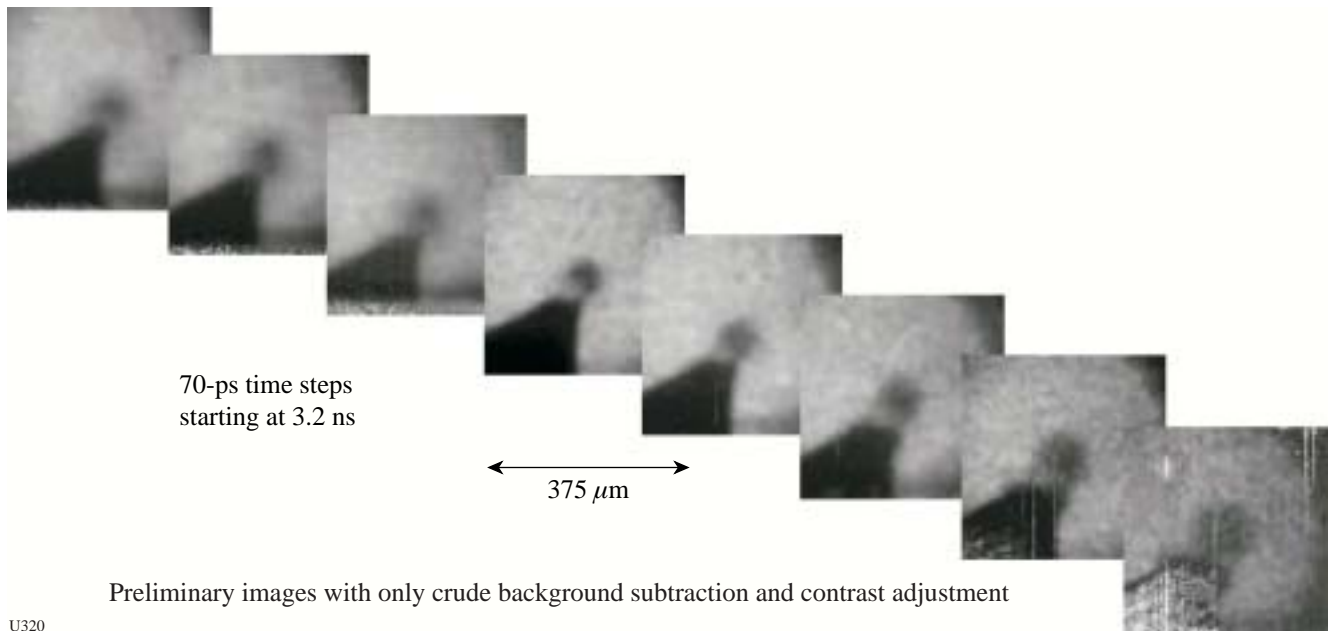


Figure 92.42

(a) Cross section of a FI cryo target designed to implode to  $\rho R \sim 2 \text{ g/cm}^2$  when driven by a 190-eV hohlraum; (b) density cross section of target at stagnation when driven symmetrically; and (c) density cross section when drive is 10% hotter on the side away from the cone.



U320

Figure 92.43

Eight of a series of 16 x-radiographs taken during a test of the cone-in-shell target design on OMEGA. The frames are 70 ps apart.

*Supernova Hydrodynamics on the OMEGA Laser.*

Principal Investigators: R. Paul Drake (University of Michigan), B. Remington (Center for Laser Astrophysics-ILSA, LLNL), and collaborators from LLNL, CEA Saclay (France), LLE, LANL, University of Arizona, University of Colorado, University of Chicago, SUNY Stony Brook, Naval Research Laboratory, and Eastern Michigan University.

The fundamental motivation for this work is that supernovae are not well understood. Recent observations have clarified the depth of this ignorance by producing observed phenomena that current theory and computer simulations cannot reproduce. Such theories and simulations involve, however, a number of physical mechanisms that have never been studied in isolation. During FY02 experiments were performed under this NLUF Program in compressible hydrodynamics and radiation hydrodynamics, relevant to supernovae and supernova remnants. These experiments produce phenomena in the laboratory that are believed, based on simulations, to be important to astrophysics but that have not been directly observed in either the laboratory or an astrophysical system. The experiments were focused on the scaling of an astrophysically relevant, radiative-precursor shock, preparations

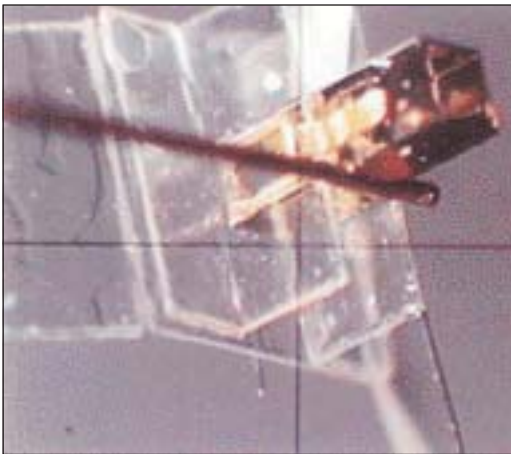
for studies of collapsing radiative shocks, and the multimode behavior and onset of turbulence in three-dimensional, deeply nonlinear evolution of the Rayleigh–Taylor (RT) instability at a decelerating, embedded interface. These experiments required strong compression and decompression, strong shocks (Mach ~10 or greater), flexible geometries, and very smooth laser beams, which means that the 60-beam OMEGA laser is the only facility capable of carrying out this program.

The experiments benefited from a strong collaborative effort that coupled a core experimental team to theoretical groups at several institutions. This enabled the development of experimental designs through advance simulations and the comparison of the results of the experiments to simulations by more than one code. A standardized approach to the experiments was also developed, enabling the pursuit of more than one experiment simultaneously, and thus the exploitation of the extensive theoretical capabilities of this collaboration. These experiments are sufficiently complex yet diagnosable, so they are excellent for verification and validation (V&V) of complex computer codes, including those produced by the Advanced Scientific Computing Initiative (ASCI) Alliance Center at the University of Chicago. This program is also a

critical stepping stone toward the use of the National Ignition Facility (NIF) both for fundamental astrophysics and as a critical component of ASCI V&V.

The supernova hydrodynamics experiments conducted in FY02 included the following:

*a. Radiative Precursor Shocks:* The scaling of radiative precursor shocks was investigated. These experiments involved the initial acceleration of a block of material to high velocity. The block of material then drove a shock wave through low-density foam at approximately 100 km/s, which was fast enough to produce a radiative precursor. The precursor is strongly sensitive to the shock velocity, so it was possible to control it by varying the laser energy. Figure 92.44 shows a photograph of a target used for experiments on OMEGA. Up to ten laser beams struck the front surface of this target, delivering several kJ of energy to an 800- $\mu\text{m}$ -diam spot in a 1-ns pulse. The laser irradiation shocked and accelerated a 60- $\mu\text{m}$ -thick plastic layer that crossed a 160- $\mu\text{m}$  vacuum gap to impact the low-density foam, usually of density 0.01 g/cm<sup>3</sup>.



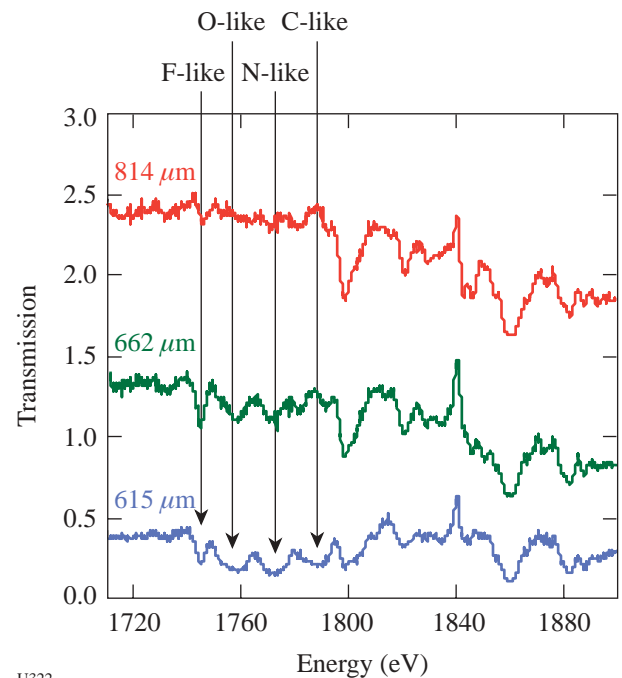
U321

Figure 92.44

An image of the target for the radiative precursor experiments. The laser beams approach from the left, driving a shock wave through the foam contained in the rectangular structure.

The structure of the precursor was investigated using absorption spectroscopy. Additional laser beams irradiated a thulium backlighter plate, permitting an imaging crystal spectrometer to obtain absorption spectra like those shown in Fig. 92.45. Absorption lines were detected from up to six

different ionization states. The lines from higher ionization states appear at higher temperatures. From the entire spectrum, one could determine the location of the shock, the temperature of the shocked material, and the temperature profile in the radiative precursor, with the help of the OPAL<sup>27</sup> atomic code. It was observed that the precursor became longer as the laser drive energy increased, and that its behavior was consistent with a simple model of the threshold velocity for the production of a precursor. A paper based on these data was recently published in Physical Review Letters.<sup>28</sup> These experiments are now entering an analysis and writing phase. In addition, it is anticipated that such experiments will provide quality benchmark cases for astrophysical modeling. Participants in such comparisons will include the University of Maryland and the ASCI Flash Center at the University of Chicago.



U322

Figure 92.45

Absorption spectra at three locations, showing the spatial development of four of the absorption lines. The spectra are offset vertically for clarity.

*b. Radiative Shocks:* Astrophysical shocks, when they become cool enough, enter a radiatively collapsing phase in which their density can increase several orders of magnitude. All supernova remnants eventually pass through this phase, and such shocks arise in a number of other contexts. This team's work with radiative-precursor shocks in foams represented a first step into radiative hydrodynamics. With the adoption of gas targets, however, shocks can be produced on OMEGA that

radiatively collapse. Several OMEGA shots were devoted to a preliminary attempt at such an experiment during FY02. They used only radiography as a diagnostic. Figure 92.46 shows the data that were obtained on the first attempt. The overlaid profile shows the average of a 290- $\mu\text{m}$ -high horizontal strip through the unobstructed portion of the image. One can clearly see the absorption feature due to the shock. Its position confirms that the shock velocity is well above 100 km/s. The laser and diagnostic settings were optimized for other experiments on this day, causing significant motional blurring (and weakening the absorption feature). Much better data can and will be obtained in future experiments. Such experiments will occupy approximately half of the target shots planned for the next year under this NLUF program.

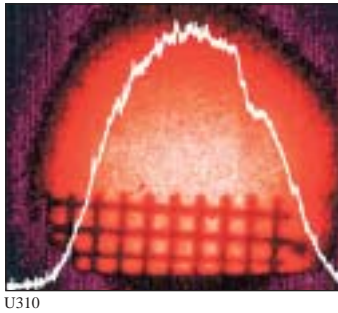


Figure 92.46  
Image and profile from a first attempt to produce a collapsing radiative shock. The notch in the profile toward the right is produced by the shocked gas.

*c. Multimode Rayleigh–Taylor (RT) Instability at a Decelerating, Embedded Interface:* It is fruitful to examine multimode systems because (a) the actual stellar explosions involve many modes and (b) the growth of multimode structures is a more-severe test of simulations. During FY02 data were obtained that showed the time evolution of the structures produced from initial conditions including one mode, two modes, and eight modes. The perturbations were designed to keep the global peak-to-valley amplitude constant at 5  $\mu\text{m}$  as the number of modes changed. Figure 92.47 shows some data that were obtained using a two-mode perturbation, and Fig. 92.48 shows some data for an eight-mode perturbation. At earlier times, the multimode data show articulated spikes. Later, as in these figures, they show the emergence of large-scale features. Additional data are needed and will be obtained soon. The emergence of the large-scale features will be compared with theories of bubble merger. The effect of the number of modes on the width of the “mix region” will also be examined.

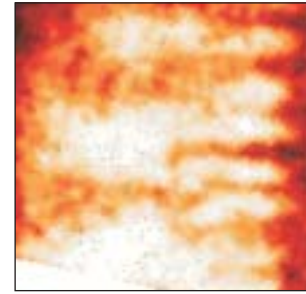


Figure 92.47  
Structures developed at 26 ns from a two-mode perturbation.

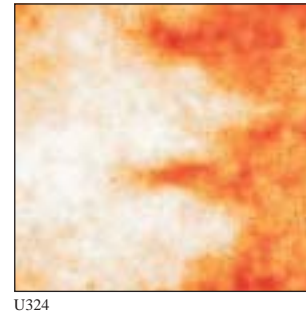


Figure 92.48  
Structures developed at 26 ns from an eight-mode perturbation.

*d. Onset of Turbulence in RT Instability at a Decelerating, Embedded Interface:* Based on a scaling analysis, it is believed that it will be possible to observe the transition to a turbulent state in the evolution of RT that develops from a 3-D initial condition. Figure 92.49 shows a radiograph of the structures produced from an initial 3-D perturbation that included a single mode with 71- $\mu\text{m}$  wavelength and noise at much shorter wavelengths introduced when the (50-mg/cc) foam was machined. By this time, the unstable fingers have developed significant modal structure and have moved forward and overtaken the shock. Earlier, the fingers have a simpler spectral structure and remain well behind the shock. Later, the ability to distinguish the fingers is lost perhaps due to rapid diffusion caused by turbulence. Continuations of these experiments will determine whether, in fact, the onset of turbulence is being observed, and further analysis will evaluate the implications for astrophysics. Several publications based on this work have appeared in print during the last year.<sup>29–31</sup> One additional manuscript has been submitted for publication.<sup>32</sup>

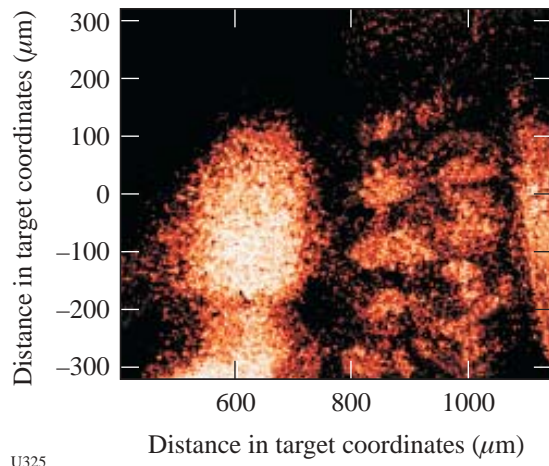


Figure 92.49

An experiment with a 3-D initial single-mode perturbation produced these structures 17 ns into the experiment.

#### *Studies of the Dynamic Properties of Shock-Compressed FCC Crystals by In-Situ Dynamic X-Ray Diffraction.*

Principal Investigators: H. Baldis (University of California at Davis), D. Kalantar (LLNL), and collaborators from LLNL, LLE, the University of California at San Diego, University of Oxford, and LANL.

This experiment uses time-resolved dynamic x-ray diffraction to investigate the response of a lattice under shock compression. Over the last two years this work included studies of shocked single-crystal Si with peak pressures ranging from <100 kbar to 200 kbar, experiments on single-crystal Cu<sup>32</sup> to study the dislocation density in the post-shocked material (these studies included recovery of shocked samples) at pressures ranging from 100 to 600 kbar, and investigations of deformation substructure in Cu.

Major accomplishments during the reporting period include the following:

- Implementation of multi-target shots. In several series of shots during this year, diffraction targets, VISAR wave profile targets, and shock-recovery targets were simultaneously fielded on shots. This approach greatly increases the effectiveness of target shots providing triple the data per shot than would have been available if the three experiments were individually shot.<sup>33</sup>

- A pressure scan for Si was completed to record multiple lattice planes.
- The wave profile of shocked Si was recorded.
- The shock breakout from 200 mm Cu was used to determine the timing for future diffraction measurements.
- Shocked crystals were recovered and examined.

In recent experiments a multiple film plane (MFP) diagnostic has been implemented that allows the observation of x-ray diffraction from a wide range of lattice planes (Fig. 92.50). The MFP has been used to record diffraction from Si shocked at a range of pressures as seen in Fig. 92.51. Figure 92.52 illustrates the analysis of such images showing a multi-wave structure that depends on intensity. A maximum of 6% compression is observed for the range of pressures attained on Nova and OMEGA in x-ray and direct-drive modes.

A two-phase approach has been adopted to analyze these data. First, the line pattern of known crystal configurations is predicted; then the diffracted lines are fit to the prediction to determine the lattice spacing and unit normal vector. An IDL code is used to calculate the expected diffraction pattern for a given crystal lattice.

#### *Optical Mixing of Controlled Stimulated Scattering Instabilities (OMC SSI) on OMEGA.*

Principal Investigator: Bedros Afeyan (Polymath Research Inc.) and collaborators from LLNL, LANL, and LLE

The goal of this experiment is to examine suppression of backscattering instabilities by the externally controlled generation of ion-acoustic-wave or electron-plasma-wave turbulence. The experiments in general consist of using optical mixing techniques to generate resonant ion-acoustic waves (IAW) in flowing plasmas created by the explosion of foils irradiated by the OMEGA laser. During this year the interaction scaling with probe intensity was examined.

The transmission of the probe beam and the Raman reflectivity of the pump beam were measured systematically for a large number of probe beam energies. The scaling of the Raman suppression with probe beam energy was examined, and transmission enhancement at low energies that saturates at high energies was observed (see Fig. 92.53). The energy transfer at high probe energies is significant, and the SRS suppression in the wavelength or plasma density window that corresponds to Mach-1 flow is suppressed significantly, upwards of factors of 8.

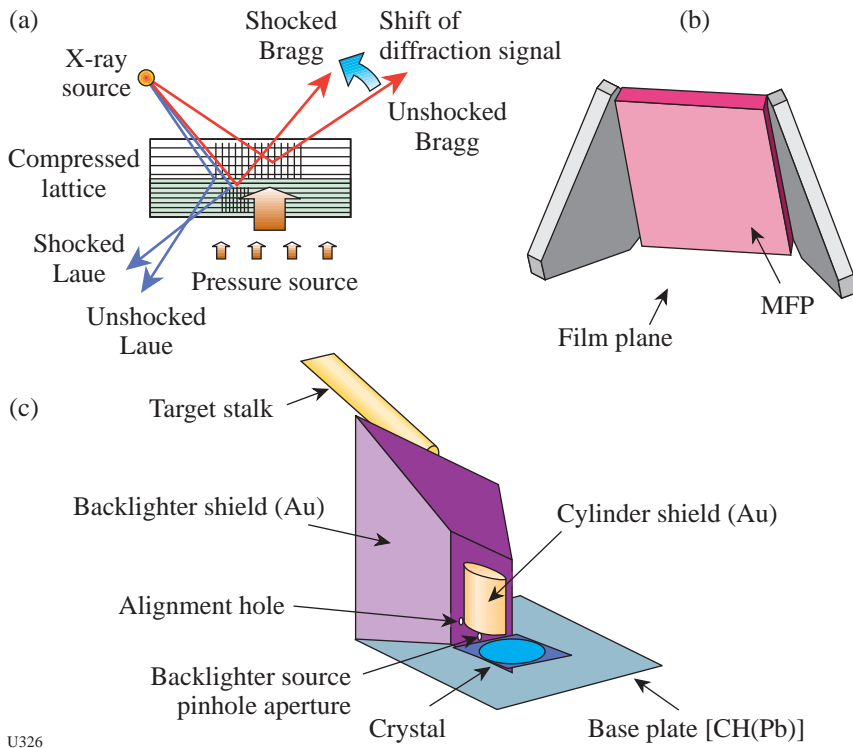
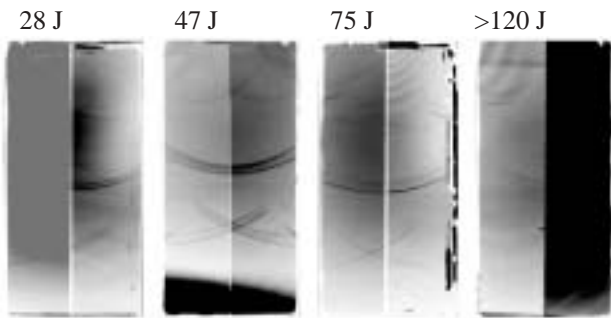


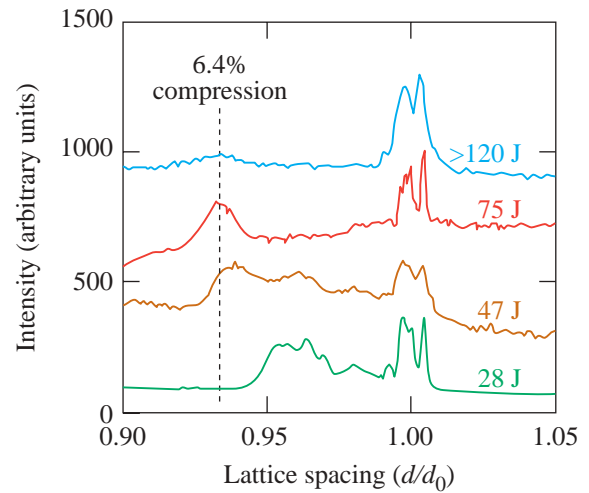
Figure 92.50  
 (a) Illustration of the concept of dynamic x-ray diffraction in probing response of crystals to laser-driven shocks; (b) schematic showing the MFP diagnostic; and (c) illustration of typical experimental configuration used on the x-ray diffraction experiments.

U326



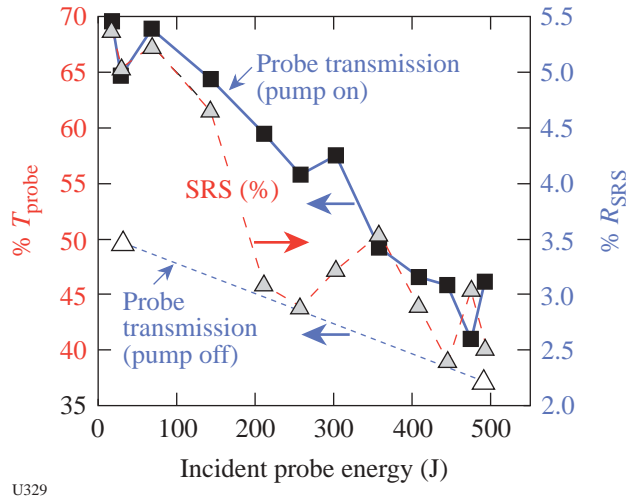
U327

Figure 92.51  
 Images of a diffracted signal from different lattice planes taken from a shocked-Si experiment on OMEGA at different laser-drive energies.



U346

Figure 92.52  
 Lineout from x-ray diffraction data of Si for various energies showing a maximum lattice compression of ~6.4%.



U329

Figure 92.53  
Measured transmission of the probe beam and the Raman reflectivity of the pump beam as a function of probe beam energy. Note that with the pump beam off, the transmission of the probe beam is less than 50%, even at moderately low energies, and decreases with energy down to less than 40% at a probe beam energy of ~490 J. The reflectivity of the pump beam falls with increasing probe energy. The energy transfer at high probe energies is significant, and the SRS suppression in the wavelength or plasma density window that corresponds to Mach-1 flow is suppressed significantly, upward of factors of 8.

**FY02 LLNL OMEGA Experimental Program**

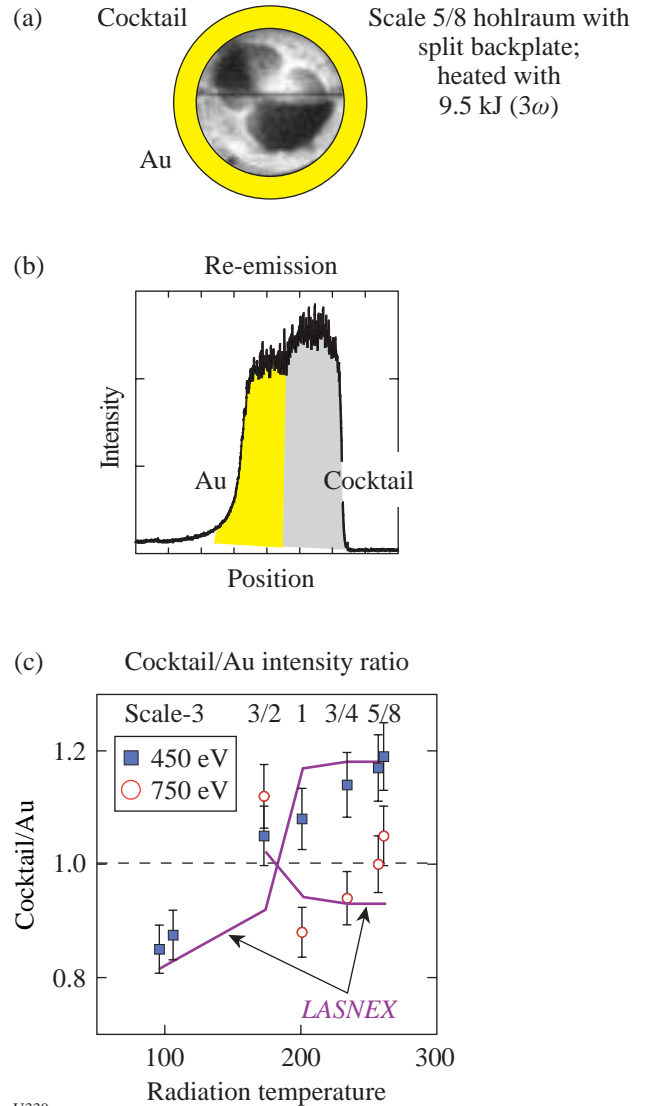
The LLNL program on OMEGA in FY02 totaled 406 target shots for target ignition physics, high-energy-density science, and NWET (Nuclear Weapons Effects Testing). This represents a 30% increase over the target shots taken by LLNL on OMEGA in FY01. Highlights of these experiments include the following:

*Laser-Plasma Interactions:* Beam-energy-transfer experiments were continued during FY02 to investigate beam-energy transfer<sup>34</sup> for a variety of NIF target/beam configurations in order to select the optimum configuration to minimize the potential deleterious effects of this process on NIF targets.

To expand the LPI (laser-plasma interaction) database on OMEGA, one of the OMEGA beamlines was modified to allow it to generate second-harmonic radiation for LPI experiments.

*Cocktail Hohlräume:* Experiments continued to investigate the potential of “cocktail” hohlraum materials to increase the soft x-ray emission and energy coupling to capsule in NIF targets. During FY02, detailed atomic physics model predic-

tions were verified on OMEGA experiments by observing enhanced cocktail re-emission at 450 eV (see Fig. 92.54).



U330

Figure 92.54  
During FY02 cocktail hohlraum experiments were conducted on OMEGA that in conjunction with LASNEX code simulations indicate that cocktail materials may be advantageous compared to Au for the NIF hohlraums. (a) Cocktail geometry; (b) experimental data from cocktail hohlraum experiment comparing Au and “cocktail” re-emission; (c) cocktail-to-Au intensity ratio at 450 eV (squares) and 750 eV (circles) plotted as a function of radiation temperature from the OMEGA experiments compared to the LASNEX predictions.

**X-Ray Thomson Scattering:** X-ray Thomson scattering can access the density/temperature parameter space that is characteristic of the Fermi degenerate to warm dense matter regime (see Fig. 92.55). OMEGA experiments have demonstrated for the first time spectrally resolved x-ray Thomson scattering

data<sup>35</sup> (Fig. 92.56). These experiments are important because they indicate that x-ray Thomson scattering may work for ICF implosions. Future experiments are planned to investigate superdense matter using this technique.

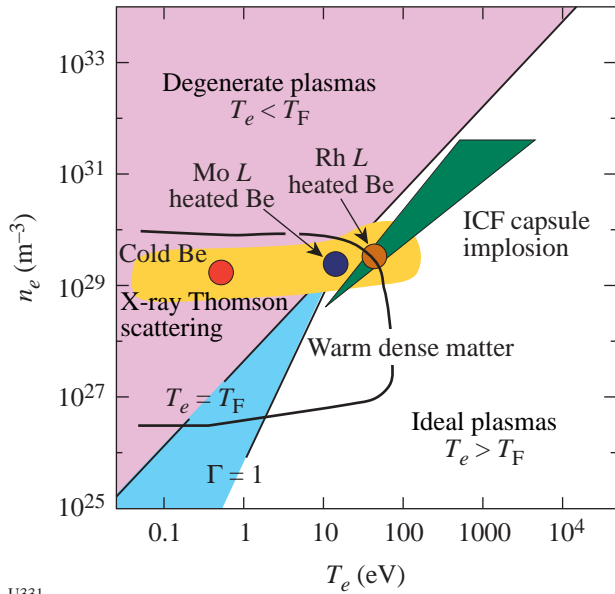


Figure 92.55  
The density and temperature space of interest to the study of dense matter showing the relevance of x-ray Thomson scattering as a diagnostic in this regime. The solid points correspond to the measurements made on the OMEGA experiments using Rh and Mo L-shell emission as a source of x-rays to conduct x-ray Thomson scattering measurements on cold and heated Be plasmas.

U331

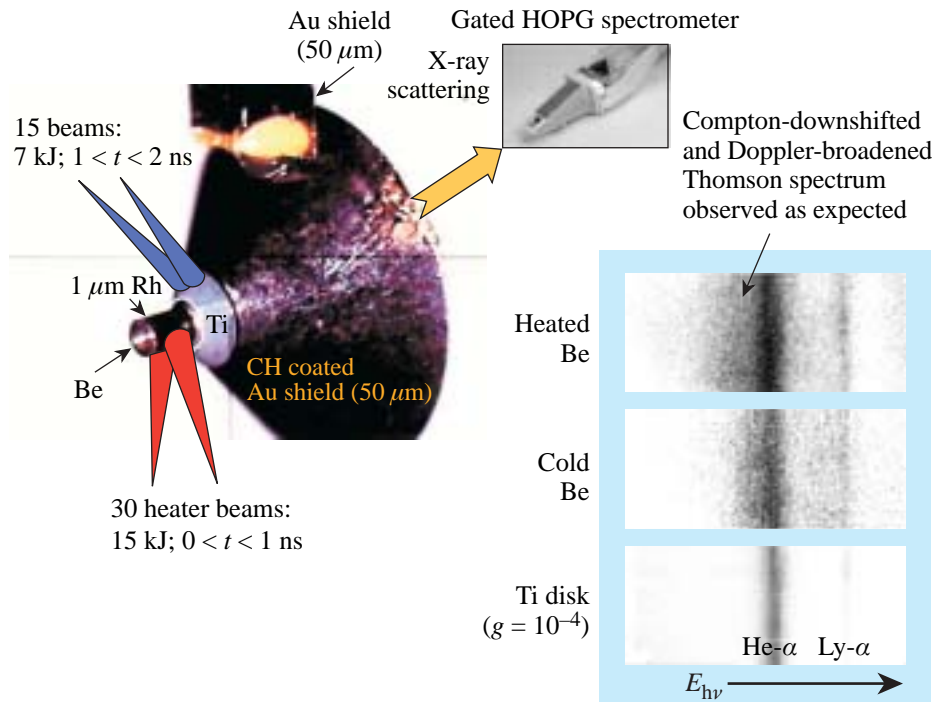


Figure 92.56  
Illustration of the x-ray Thomson scattering experiment on OMEGA. Thirty OMEGA beams are used as heater beams to heat a Be plasma. A separate x-ray source is used to probe the hot plasma and produces the scattered Ti-disk spectrum irradiated with up to 15 beams (at the right).

U332

*Albedo Experiments:* A series of experiments were initiated in FY02 on OMEGA to measure the absolute albedo of a secondary hohlraum as shown in Fig. 92.57. Three detectors are used in this measurement: DANTE, a PCD in H11, and a PCD in P11. DANTE is the primary diagnostic, while the P11 PCD monitors the effect of the secondary hohlraum and the H11 PCD serves as backup for the DANTE measurement. Initial measurements confirmed that the secondary hohlraum has no significant effect on the primary's radiation temperature. In measurements comparing the albedo of Au and U, the Au albedo was observed to be smaller than that of U.

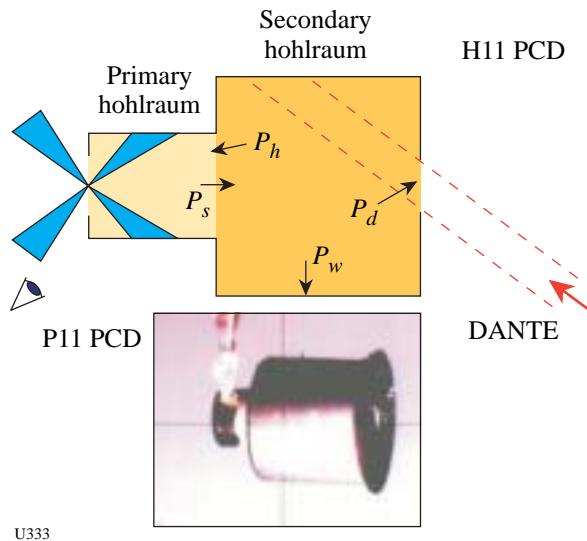


Figure 92.57 Schematic of the “Albedo” experiment. A half-hohlraum is irradiated by a set of OMEGA beams and provides radiation that heats a secondary hohlraum attached to its back. DANTE is the primary diagnostic viewing the wall of the secondary hohlraum; the H11 PCD is a backup for DANTE. The P11 PCD monitors the primary hohlraum to determine the effect of the secondary on its radiation temperature.

*Hot Hohlraum:* A series of experiments are underway on OMEGA to produce high-radiation-temperature hohlraums by reducing the scale size of the hohlraums. Hot hohlraums are needed for NIF opacity experiments, but their physics regime is not well understood. Scaled experiments at OMEGA are used to compare experimental results to theoretical models. The laser coupling to the hohlraum was determined as a function of scale size by measuring x-ray drive, backscatter,

and intensity of hot electrons. Scale-1/2 and -1/4 hohlraums were driven in a half-hohlraum configuration, and radiation temperatures of ~350 eV were demonstrated.

*Gas-Filled Radiation Sources:* Experiments continued under an NWET program to develop high-efficiency x-ray sources for the NIF. During FY02 the experiments were designed to explore x-ray emission in the >10-keV region. Typical targets included Kr-filled CH cans (1.2 mm long, 1.5 mm in diameter). Figure 92.58 shows time-framed x-ray images from two experiments with 0.5-atm- and 1.5-atm-Kr-filled cans. X-ray emission is observed from the full extent of the can (1.2-mm × 1.5-mm diameter) and beyond the duration of the 1-ns laser pulse in both cases.

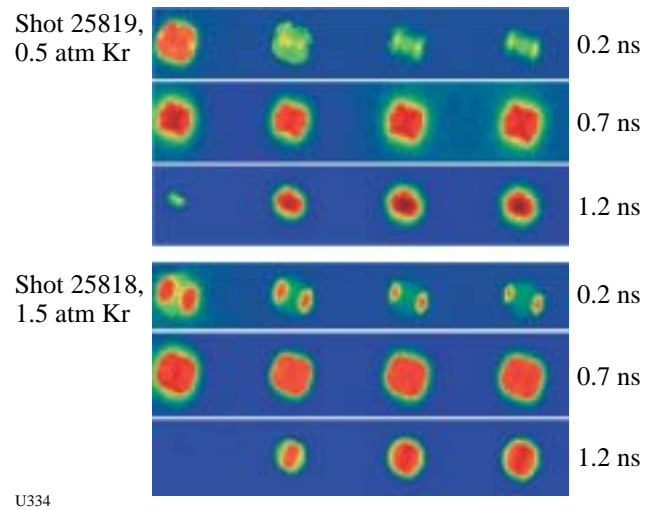


Figure 92.58 X-ray framing camera images from shot 25819 (0.5 atm Kr) and 25818 (1.5 atm Kr) show the pressure dependence in the evolution of >10-keV x-ray emission. The times are referenced to the start of the ~1-ns-long laser pulse.

*Dynamic Hohlraums:* A series of experiments dubbed “dynamic hohlraums” were carried out on OMEGA in direct-drive mode. These experiments were designed to image a radiatively collapsed shock. The configuration is shown schematically in Fig. 92.59. A gas-filled CH shell is irradiated directly by 40 OMEGA beams. To achieve as uniform a drive as possible with only 40 polar beams, the polar-beam energies are lowered in comparison to the rest of the beams. Typical data from these implosions are shown in Fig. 92.60.

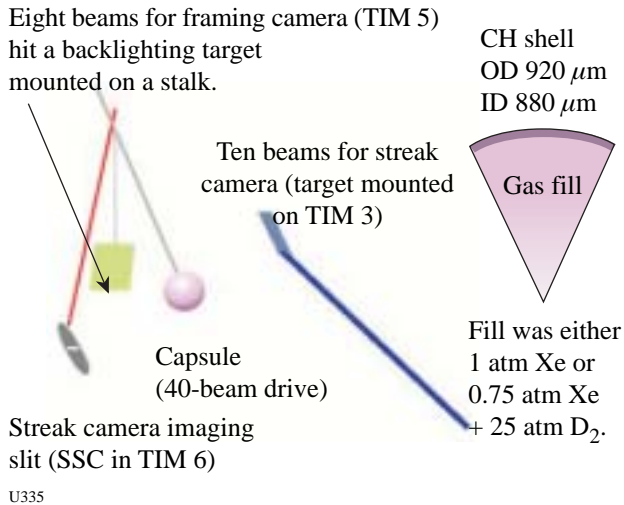


Figure 92.59  
Schematic illustration of the “dynamic hohlraum” direct-drive implosion experiment designed to image a radiatively collapsed shock.

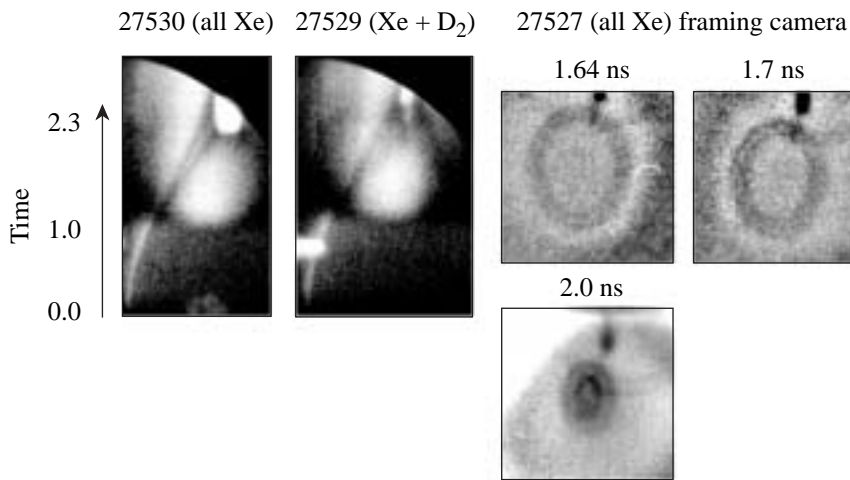
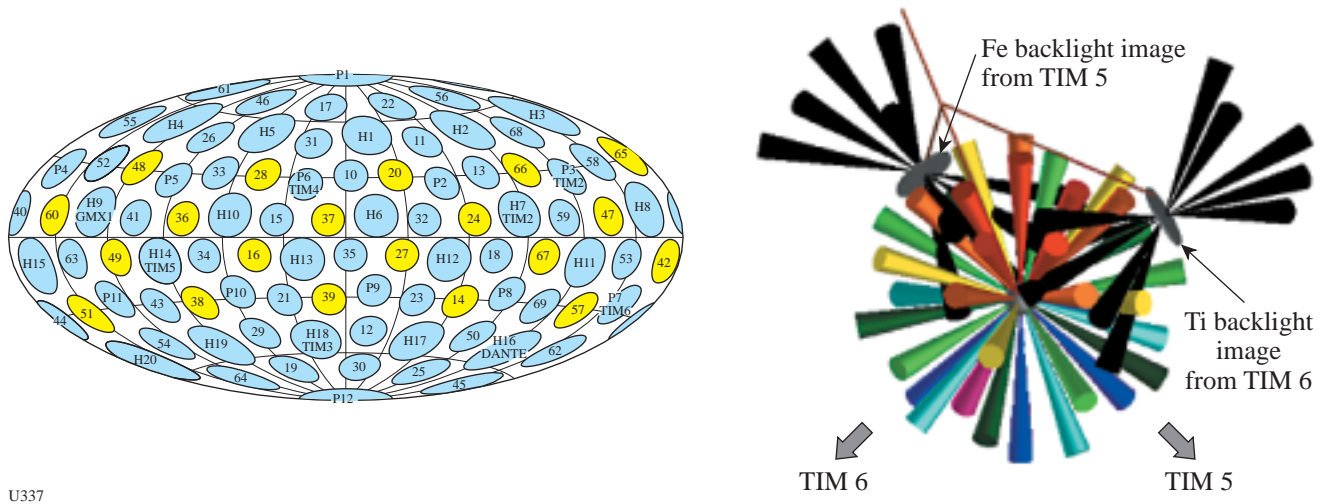


Figure 92.60  
Streaked (left) and gated (right) x-ray images of x-ray-backlit implosions of Xe- and Xe/D<sub>2</sub>-filled CH shells. The separation between the plastic shell and the collapsed shock is discernable in shots with Xe fill but not on shots with partial D<sub>2</sub> fills

*Nonideal Implosions:* The nonideal implosion (NIBI) experiment is designed to study highly distorted implosions. This experiment, carried out on OMEGA in FY02, used the direct-drive configuration shown in Fig. 92.61.

Experiments were carried out with symmetrical capsules as well as machined capsules with a 50° radiographic tracer “cap” as shown in Fig. 92.62.

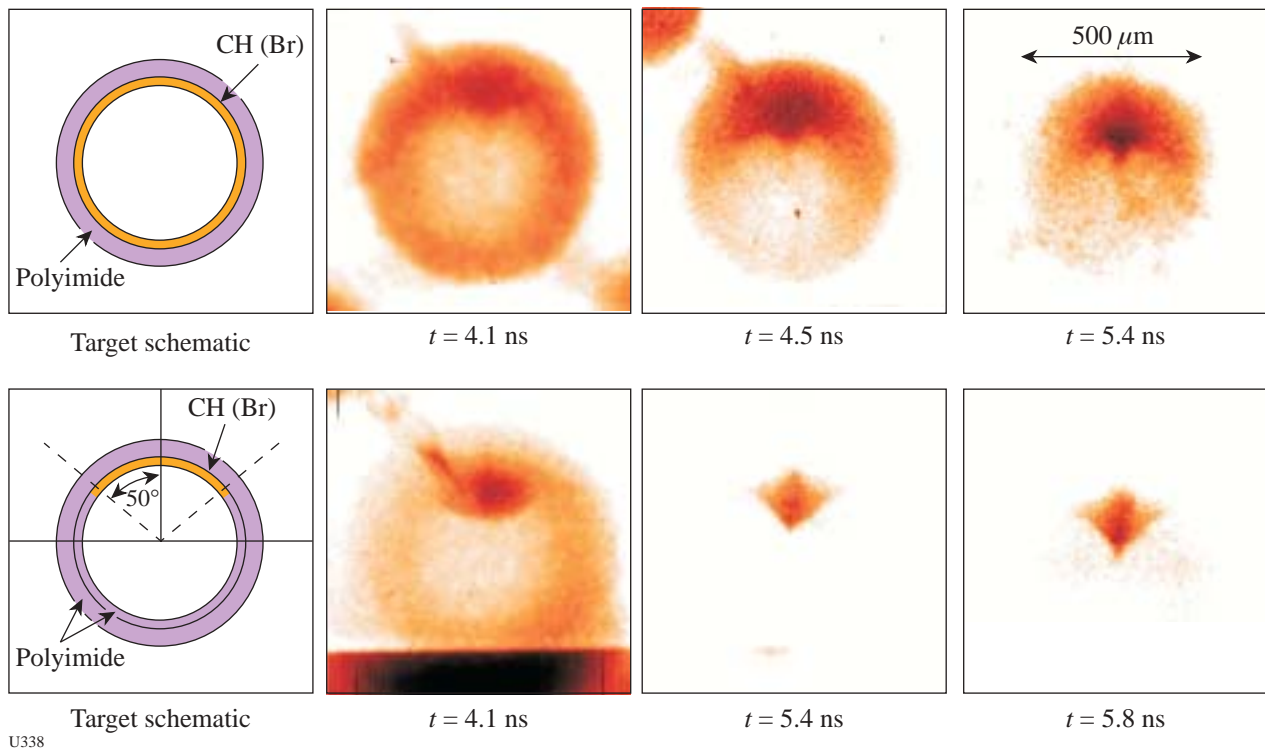
*Double-Shell Implosion Experiments:* The effect of Au M-band asymmetry on the implosion of double-shell capsules is being investigated on OMEGA. The motivation for this work is that 80% of the radiation reaching the inner shell in a double-shell configuration is 2 to 4 keV Au “M-band” radiation. Simulations indicate that the inner glass shell will suffer an ~25% distortion from an ~10% P2 M-band asymmetry at a convergence of ~60%. To ameliorate this problem, an elongated hohlraum configuration is being explored.



U337

Figure 92.61

System configuration for the OMEGA NIBI experiment. Forty OMEGA beams are used to drive the implosion while twenty beams are used to produce two separate backlighting views. The forty drive beams can be adjusted to produce various asymmetric drive configurations. The beams indicated in yellow on the left are used for the two backlighting views.



U338

Figure 92.62

Target schematics (left top and bottom) for some of the NIBI implosion targets. The time-gated x-ray-backlit images on the right show the evolution of the core asymmetry when the targets are driven with a strong  $\ell = 1$  mode (higher energy on the top pole).

*Charged-Particle Spectrometry in Indirect-Drive Implosions:*

To assess the effectiveness of charged-particle spectrometry on the NIF, a collaborative experiment involving LLNL, MIT PSFC, and LLE was implemented on OMEGA in FY02. During the experiment D<sup>3</sup>He-filled shells were imploded in a conventional hohlraum configuration. Wedged-range-filter (WRF) spectrometers were used to measure the yield, spectrum, and spatial distribution of primary D<sup>3</sup>He protons. Initial results from these shots indicate that capsule areal density can be measured with this configuration. When viewed through a diagnostic hole in the hohlraum, the proton slowing down indicated a capsule  $\rho R \sim 42 \pm 9$  mg/cm<sup>2</sup> compared to a predicted areal density of  $\sim 49$  mg/cm<sup>2</sup>. No large asymmetries in proton emission were observed. It was concluded that charged-particle spectrometry can be an important diagnostic technique for indirect-drive targets. Improvements in the diagnostic were suggested by the results of these experiments to optimize the technique for indirect-drive experiments.

*IDrive:* Work continued on OMEGA in FY02 to implement the IDrive technique as a high-pressure drive technique for materials studies. One of the goals of this program is to measure the material strength of solid aluminum (6061) at peak pressures of  $\sim 300$  kbar. The experiments include soft recovery of accelerated foils in order to provide the opportunity for microscopic analysis of the highly strained regions of the materials.

**FY02 LANL OMEGA Experimental Program**

The LANL program on OMEGA in FY02 continued experiments in support of stockpile stewardship (ACE), cylindrical mix (CYLMIX), and double-shell implosion campaigns and began the asymmetric direct-drive sphere (ADDS) campaign. LANL continued NIF phase-2 diagnostic development and also collaborated with a large national group on the hydrodynamic jet experiment. LANL also provided shock-breakout measurements for the Sandia National Laboratory (SNL) ablator characterization campaign. Each of these experimental campaigns has been documented in pre- and post-shot reports. Highlights of these experiments include the following:

*ACE Experiments:* The ACE experiments successfully obtained data in support of the Stockpile Stewardship Program. This year a new backlighter configuration was developed that provides views of the experiment at two different times, thus increasing the efficiency of the experiments. In collaboration with AWE, a fluorescence-based spectro-meter was fielded to measure temperatures in radiation-driven experiments.

*Asymmetric Direct-Drive Spheres:* The goal of the asymmetric direct-drive spheres (ADDS) campaign is to elucidate the effect of mix on imploding capsules. The experiment uses directly driven DT-filled capsules. The energies of each laser beam are adjusted so that the capsule sees a positive or negative drive asymmetry as measured by the second Legendre mode. Theoretical calculations predict a difference in neutron yield and core shape, depending on the sign and magnitude of the asymmetry. The primary diagnostics of mix are neutron yield, imaging of the emitted neutrons, and x-ray imaging (in collaboration with LLE).

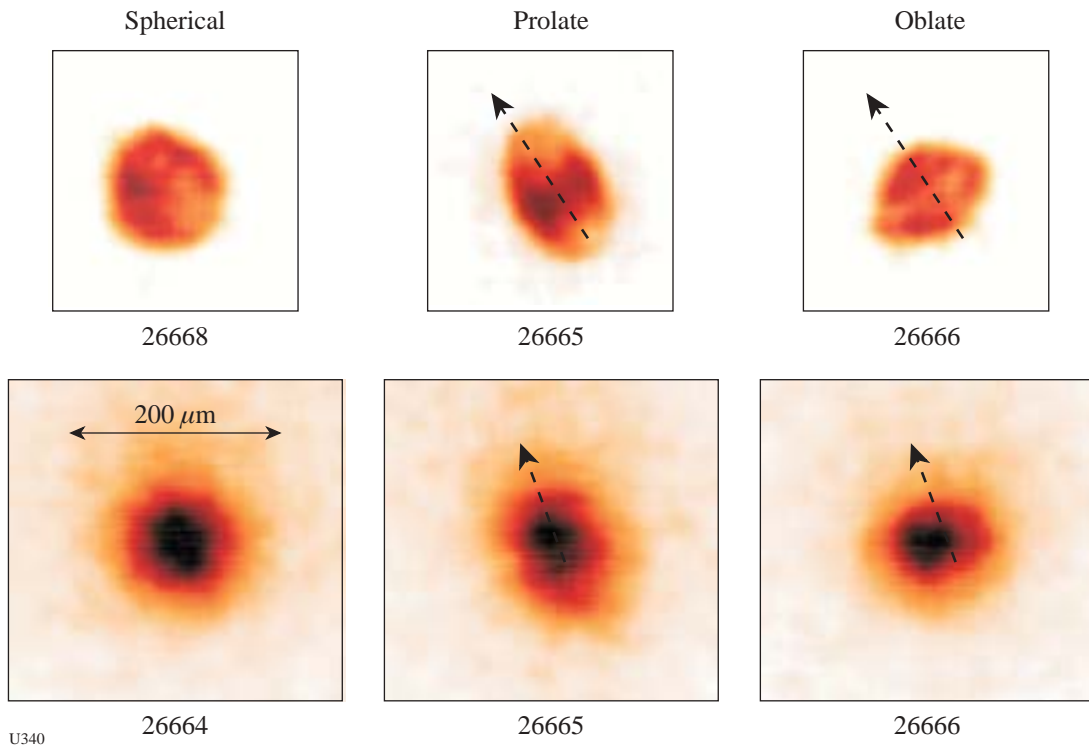
Figure 92.63 presents the first simultaneous neutron and x-ray images of asymmetric implosions. The predicted shapes and neutron yields agree with the measurements in direction and magnitude.

*CYLMIX:* The Richtmyer–Meshkov instability occurs whenever a strong shock passes through an interface between two materials. The CYLMIX experiments study this instability under unique convergent, compressible, miscible plasma conditions in the presence of a strong (Mach number greater than 5) shock. To produce a strong shock, small plastic cylinders (Fig. 92.64) are directly driven by the OMEGA laser.<sup>36</sup> The implosion trajectory has been carefully mapped and simulations tuned to match the measurements, as in Fig. 92.65.

As the cylinders implode, the marker band mixes into the surrounding material and the mix width is measured. This year, extensive measurements spanning several nanoseconds were made of the dependence of the mix width on the initial surface roughness of the marker layer as a function of time. Comparisons with simulations to validate hydrodynamic models have been made.

*Hydrodynamic Jet Experiment:* LANL also participated in a large collaboration that includes researchers from LLNL, AWE, LLE, U. Michigan, and NRL to simulate jets in supernova explosions.<sup>37</sup> Astrophysical codes will be validated by comparison to OMEGA experimental data. The experiments are presently optimizing the target and diagnostics while design work linking 2-D *DLASNEX* calculations to the radiation-hydrodynamic code *RAGE* is underway. Exploratory experiments were conducted this year.

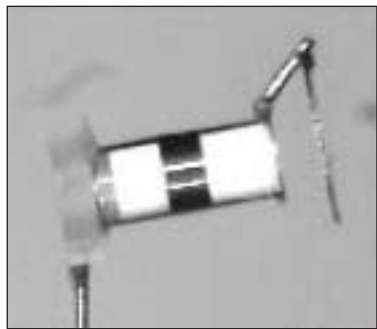
*NIF Diagnostics:* Development continued on Phase 2 fusion product diagnostics for the NIF. A second Gas–Cerenkov gamma-ray burn-history diagnostic, with increased time reso-



U340

Figure 92.63

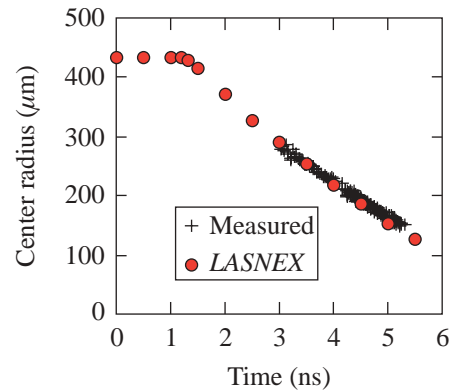
X-ray (top) and neutron (bottom) images for three different degrees of asymmetric drive. The x-ray images are from the GMXI diagnostic, and the 14.1-MeV neutron images were obtained in a LANL/CEA/LLE collaboration. All images are as seen by the diagnostic. The arrows indicate the perturbation axis.



U341

Figure 92.64

A view of a typical CYLMIX target from the side showing the backlighter disk on the right, the Al marker band in the middle, the foam inside the cylinder (white areas), and the viewing aperture on the left. The primary diagnostic is an x-ray framing camera with a line of sight down the axis of the cylinder.



U342

Figure 92.65

Measured radius versus time plot demonstrating good modeling of the experiment.

lution, was built and fielded in conjunction with LLNL. Development continued on the neutron imaging system (NIS), which was a primary diagnostic for the ADDS experiment, as illustrated in Fig. 92.63. The NIS is fielded in collaboration with CEA and LLE.

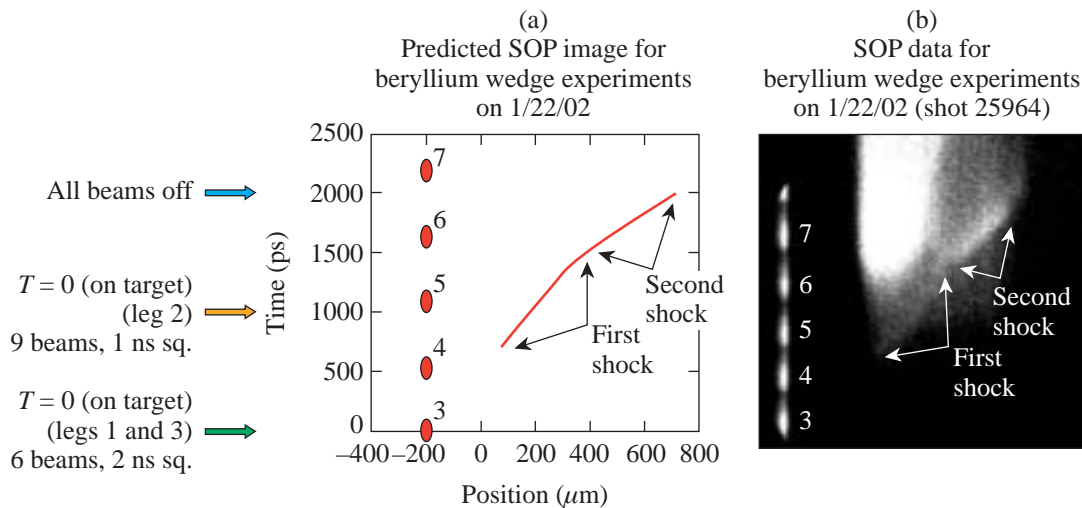
**FY02 SNL OMEGA Programs**

SNL carried out a total of 24 target shots on the OMEGA laser in FY02 and also participated in several of the campaigns led by other laboratories. The SNL-led campaigns included the following:

*Indirect-Drive Ablator Shock Coalescence:* The achievement of indirect-drive ignition of a NIF capsule requires capsule shock timing precision of ~150 ps. The first attempts at time-resolved measurement of the coalescence of two shocks (at pressures of ~10 and 50 Mbar, respectively) in a Be + 0.9% Cu wedge ablator were made in a collaborative effort involving SNL and LANL. The principal diagnostic was the LANL Streaked Optical Pyrometer (SOP).<sup>38</sup> The hohlraum drive for this experiment consisted of a 2-ns square pulse in six beams followed by a 1-ns square pulse in nine beams delayed by 1 ns. As shown in Fig. 92.66, shock coalescence occurred within about 300 ps of the pre-shot calculation.

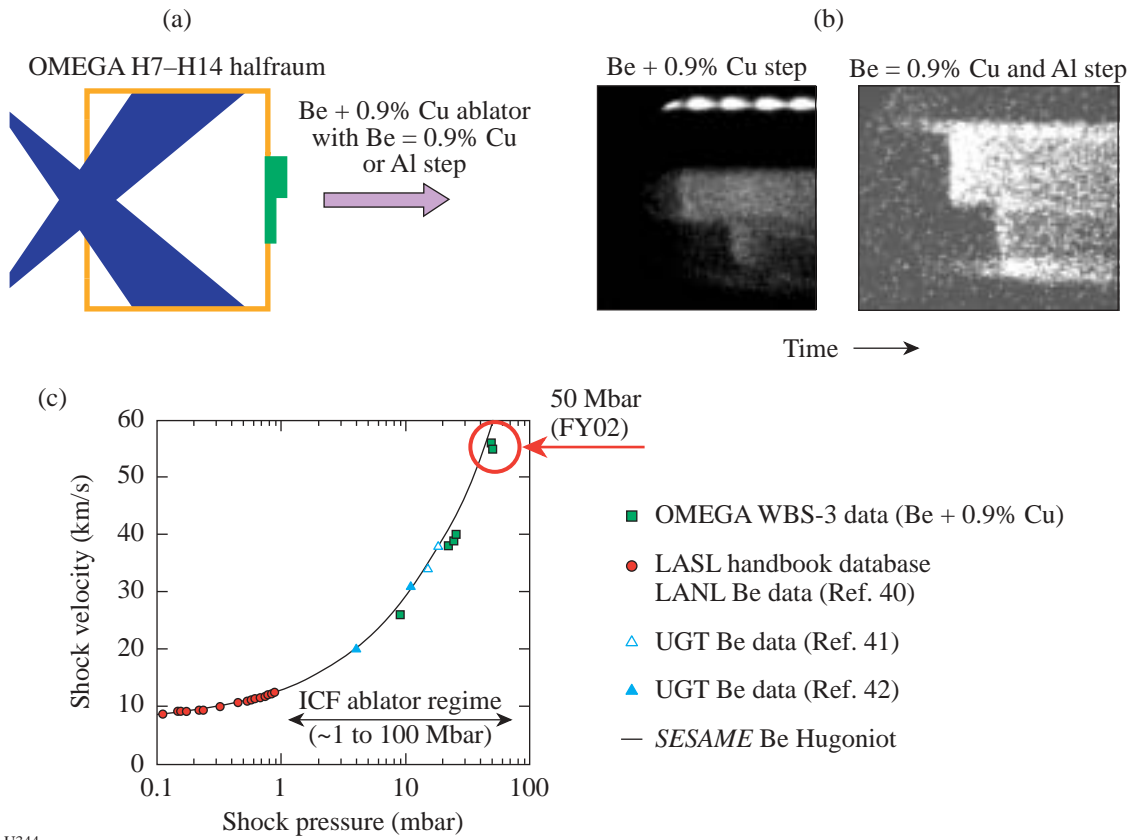
*Indirect-Drive Ablator Shock Velocity at 50 Mbar:* The achievement of indirect-drive ignition of a NIF capsule requires capsule ablation pressures in the range of 1 to 100 Mbars. In FY02 SNL/LANL experiments on OMEGA extended the shock velocity data for Be + 0.9% Cu ablator samples to the 50-Mbar level<sup>39</sup> (Fig. 92.67). Shock velocities in the ablator were measured with Be + 0.9% Cu step samples. Al step witness plates were also used to confirm the shock pressure levels generated in the Be + 0.9% Cu ablator samples.

*Indirect-Drive Ablator X-Ray Burnthrough Measurements:* To achieve indirect-drive ignition of a NIF capsule, ablator burnthrough timing must be predicted to within a few percent. In FY02 SNL/LLNL experiments on OMEGA extended the x-ray burnthrough<sup>39</sup> data for polyimide and Be + 0.9% Cu ablators into the range of 190- to 200-eV hohlraum temperatures. As shown in Fig. 92.68, the experimental technique provides simultaneous measurements of ablator x-ray burnthrough and x-ray re-emission (in the interior of the hohlraum). As shown in the figure, experimental arrangements involving multiple sample regions were also tested in the FY02 experiments.



U343

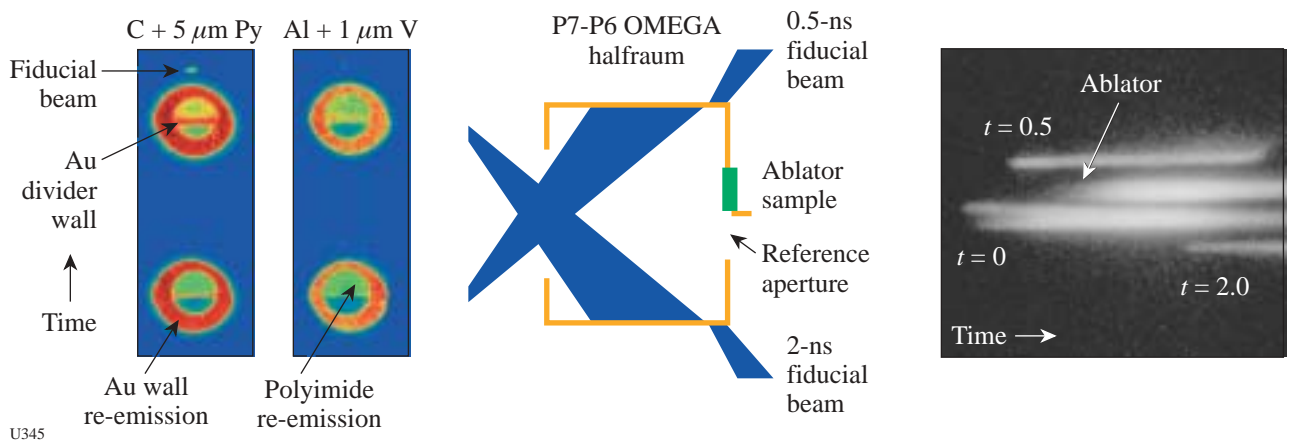
Figure 92.66  
 Predicted (a) and actual (b) shock coalescence as measured with SOP.



U344

Figure 92.67

(a) Schematic illustrating the setup of a shock velocity measurement experiment. A step target is mounted on the back of a half-hohlraum that is irradiated by a subset of OMEGA beams. (b) Experimental data from two shock velocity measurement experiments. (c) Plot of shock velocity versus shock pressure from the OMEGA experiments compared to data from other sources in the ICF-ablator-relevant regime of interest.



U345

Figure 92.68

Schematic illustrating the ablator burnthrough measurement technique used on the SNL experiments on OMEGA.

*Time and Spatially Resolved Measurements of X-Ray Burnthrough and Re-emission in Au and Au:Dy:Nd Foils:* A mixture containing two or more high-Z elements can result in a material with a higher Rosseland mean opacity than either of the constituents. Computational simulations of the x-ray re-emission properties of such "cocktail" materials indicate that wall losses in a National Ignition Facility (NIF) ignition-scale hohlraum could be reduced by a significant amount (when compared to walls made of pure Au).<sup>43</sup> In a recent set of experiments on OMEGA a collaborative team including SNL, LLNL, and GA used x-ray framing and streak cameras to simultaneously measure the x-ray burnthrough and re-emission of pure Au and Au:Dy:Nd cocktail samples exposed to a hohlraum radiation temperature of ~160 eV. Although the burnthrough measurements indicate the cocktail has a higher Rosseland mean opacity than pure Au, the measured x-ray re-emission fluxes from the two materials were approximately equivalent.

## CEA

CEA had four half-day dedicated shot opportunities on OMEGA during FY02. A total of 19 target shots were provided for experiments including tests of the LMJ three-ring symmetry and other aspects of indirect-drive targets. In addition, CEA participated in collaborative experiments on imaging the neutron core emission using the CEA-provided neutron-imaging system (NIS).<sup>44</sup>

## REFERENCES

1. B. Yaakobi, F. J. Marshall, and D. K. Bradley, *Appl. Opt.* **37**, 8074 (1998).
2. S. W. Haan *et al.*, *Phys. Plasmas* **2**, 2480 (1995).
3. J. D. Lindl, R. L. McCrory, and E. M. Campbell, *Phys. Today* **45**, 32 (1992).
4. *Energy and Technology Review*, Lawrence Livermore National Laboratory, Livermore, CA, UCRL-52000-94-12, 1 (1994).
5. M. D. Rosen, *Phys. Plasmas* **3**, 1803 (1996).
6. M. Andre, M. Novaro, and D. Schirmann, *Chocs* **13**, 73 (1995); J. Maddox, *Nature* **372**, 127 (1994).
7. C. K. Li, D. G. Hicks, F. H. Séguin, J. A. Frenje, R. D. Petrasso, J. M. Soures, P. B. Radha, V. Yu. Glebov, C. Stoeckl, D. R. Harding, J. P. Knauer, R. L. Kremens, F. J. Marshall, D. D. Meyerhofer, S. Skupsky, S. Roberts, C. Sorce, T. C. Sangster, T. W. Phillips, M. D. Cable, and R. J. Leeper, *Phys. Plasmas* **7**, 2578 (2000).
8. F. H. Séguin, J. A. Frenje, C. K. Li, D. G. Hicks, S. Kurebayashi, J. R. Rygg, B.-E. Schwartz, R. D. Petrasso, S. Roberts, J. M. Soures, D. D. Meyerhofer, T. C. Sangster, C. Sorce, V. Yu. Glebov, C. Stoeckl, T. W. Phillips, R. J. Leeper, K. Fletcher, and S. Padalino, "Spectrometry of Charged Particles from Inertial-Confinement-Fusion Plasmas," to be published in the *Review of Scientific Instruments*.
9. F. H. Séguin, C. K. Li, D. G. Hicks, J. A. Frenje, K. M. Green, R. D. Petrasso, J. M. Soures, D. D. Meyerhofer, V. Yu. Glebov, C. Stoeckl, P. B. Radha, S. Roberts, C. Sorce, T. C. Sangster, M. D. Cable, S. Padalino, and K. Fletcher, *Phys. Plasmas* **9**, 2725 (2002).
10. F. H. Séguin, C. K. Li, J. A. Frenje, S. Kurebayashi, R. D. Petrasso, F. J. Marshall, D. D. Meyerhofer, J. M. Soures, T. C. Sangster, C. Stoeckl, J. A. Delettrez, P. B. Radha, V. A. Smalyuk, and S. Roberts, *Phys. Plasmas* **9**, 3558 (2002).
11. R. D. Petrasso, C. K. Li, M. D. Cable, S. M. Pollaine, S. W. Haan, T. P. Bernat, J. D. Kilkenny, S. Cremer, J. P. Knauer, C. P. Verdon, and R. L. Kremens, *Phys. Rev. Lett.* **77**, 2718 (1996).
12. D. D. Meyerhofer, J. A. Delettrez, R. Epstein, V. Yu. Glebov, V. N. Goncharov, R. L. Keck, R. L. McCrory, P. W. McKenty, F. J. Marshall, P. B. Radha, S. P. Regan, S. Roberts, W. Seka, S. Skupsky, V. A. Smalyuk, C. Sorce, C. Stoeckl, J. M. Soures, R. P. J. Town, B. Yaakobi, J. D. Zuegel, J. Frenje, C. K. Li, R. D. Petrasso, D. G. Hicks, F. H. Séguin, K. Fletcher, S. Padalino, M. R. Freeman, N. Izumi, R. Lerche, T. W. Phillips, and T. C. Sangster, *Phys. Plasmas* **8**, 2251 (2001).
13. D. D. Meyerhofer, J. A. Delettrez, R. Epstein, V. Yu. Glebov, V. N. Goncharov, R. L. Keck, R. L. McCrory, P. W. McKenty, F. J. Marshall, P. B. Radha, S. P. Regan, S. Roberts, W. Seka, S. Skupsky, V. A. Smalyuk, C. Sorce, C. Stoeckl, J. M. Soures, R. P. J. Town, B. Yaakobi, J. Frenje, C. K. Li, R. D. Petrasso, F. H. Séguin, K. Fletcher, S. Padalino, C. Freeman, N. Izumi, R. A. Lerche, T. W. Phillips, and T. C. Sangster, *Plasma Phys. Control. Fusion* **43**, A277 (2001).
14. P. B. Radha, J. Delettrez, R. Epstein, V. Yu. Glebov, R. Keck, R. L. McCrory, P. McKenty, D. D. Meyerhofer, F. Marshall, S. P. Regan, S. Roberts, T. C. Sangster, W. Seka, S. Skupsky, V. Smalyuk, C. Sorce, C. Stoeckl, J. Soures, R. P. J. Town, B. Yaakobi, J. Frenje, C. K. Li, R. D. Petrasso, F. H. Séguin, K. Fletcher, S. Padalino, C. Freeman, N. Izumi, R. Lerche, and T. W. Phillips, *Phys. Plasmas* **9**, 2208 (2002).
15. C. K. Li, F. H. Séguin, J. A. Frenje, S. Kurebayashi, R. D. Petrasso, D. D. Meyerhofer, J. M. Soures, J. A. Delettrez, V. Yu. Glebov, P. B. Radha, F. J. Marshall, S. P. Regan, S. Roberts, T. C. Sangster, and C. Stoeckl, *Phys. Rev. Lett.* **89**, 165002 (2002).
16. C. K. Li, F. H. Séguin, D. G. Hicks, J. A. Frenje, K. M. Green, S. Kurebayashi, R. D. Petrasso, D. D. Meyerhofer, J. M. Soures, V. Yu. Glebov, R. L. Keck, P. B. Radha, S. Roberts, W. Seka, S. Skupsky, C. Stoeckl, and T. C. Sangster, *Phys. Plasmas* **8**, 4902 (2001).
17. V. A. Smalyuk, V. N. Goncharov, J. A. Delettrez, F. J. Marshall, D. D. Meyerhofer, S. P. Regan, and B. Yaakobi, *Phys. Rev. Lett.* **87**, 155002 (2001).
18. T. R. Boehly, D. L. Brown, R. S. Craxton, R. L. Keck, J. P. Knauer, J. H. Kelly, T. J. Kessler, S. A. Kumpan, S. J. Loucks, S. A. Letzring, F. J. Marshall, R. L. McCrory, S. F. B. Morse, W. Seka, J. M. Soures, and C. P. Verdon, *Opt. Commun.* **133**, 495 (1997).

19. R. A. Lerche, D. W. Phillion, and G. L. Tietbohl, *Rev. Sci. Instrum.* **66**, 933 (1995).
20. R. D. Petrasso, C. K. Li, F. H. Séguin, J. A. Frenje, S. Kurebayashi, P. B. Radha, D. D. Meyerhofer, J. M. Soares, J. A. Delettrez, C. Stoeckl, S. Roberts, V. Yu. Glebov, W. Seka, C. Chiritescu, and T. C. Sangster, *Bull. Am. Phys. Soc.* **46**, 105 (2001).
21. C. K. Li and R. D. Petrasso, *Phys. Rev. Lett.* **70**, 3059 (1993).
22. From other D<sup>3</sup>He implosion experiments for which the signals are similar in amplitude to those of Fig. 92.38(b), the presence of the shock yield is clearly visible, so the absence of the shock yield in Fig. 92.38(b) is not due to lack of instrument sensitivity.
23. E. Goldman, Laboratory for Laser Energetics Report No. 16, University of Rochester (1973).
24. R. K. Fisher, R. B. Stephens, L. Disdier, J. L. Bourgade, A. Rouyer, P. A. Jaanimagi, T. C. Sangster, R. A. Lerche, and N. Izumi, *Phys. Plasmas* **9**, 2182 (2002).
25. M. Tabak *et al.*, *Phys. Plasmas* **1**, 1626 (1994).
26. P. A. Norreys *et al.*, *Phys. Plasmas* **7**, 3721 (2000).
27. C. A. Iglesias and F. J. Rogers, *Astrophys. J.* **464**, 943 (1996); F. J. Rogers, F. J. Swenson, and C. A. Iglesias, *Astrophys. J.* **456**, 902 (1996).
28. P. A. Keiter, R. P. Drake, T. S. Perry, H. F. Robey, B. A. Remington, C. A. Iglesias, R. J. Wallace, and J. Knauer, *Phys. Rev. Lett.* **89**, 165003 (2002).
29. R. P. Drake and P. A. Keiter, *Phys. Plasmas* **9**, 382 (2002).
30. R. P. Drake, H. F. Robey, O. A. Hurricane, H. Zhang, B. A. Remington, J. Knauer, J. Glimm, D. Arnett, J. O. Kane, K. S. Budil, and J. Grove, *Astrophys. J.* **564**, 896 (2002).
31. C. Calder *et al.*, *Astrophys. J. Suppl. Ser.* **143**, 201 (2002).
32. H. F. Robey *et al.*, "The Onset of Turbulence in High Reynolds Number, Accelerated Flows. Part II. Experiment," submitted to *Physics of Fluids*.
33. M. A. Meyers *et al.*, in *Shock Compression of Condensed Matter, AIP Conference Proceedings 620* (American Institute of Physics, New York, 2001), pp. 619–622; D. H. Kalantar *et al.*, in *Shock Compression of Condensed Matter, AIP Conference Proceedings 620* (American Institute of Physics, New York, 2001), pp. 615–618.
34. R. K. Kirkwood, J. D. Moody, A. B. Langdon, B. I. Cohen, E. A. Williams, M. R. Dorr, J. A. Hittinger, R. Berger, P. E. Young, L. J. Suter, L. Divol, S. H. Glenzer, O. L. Landen, and W. Seka, *Phys. Rev. Lett.* **89**, 215003 (2002).
35. S. H. Glenzer *et al.*, *Bull. Am. Phys. Soc.* **47**, 63 (2002); G. Gregori *et al.*, *ibid.*
36. C. W. Barnes, S. H. Batha, A. M. Dunne, G. R. Magelssen, S. Rothman, R. D. Day, N. E. Elliott, D. A. Haynes, R. L. Holmes, J. M. Scott, D. L. Tubbs, D. L. Youngs, T. R. Boehly, and P. A. Jaanimagi, *Phys. Plasmas* **9**, 4431 (2002).
37. J. M. Foster *et al.*, *Phys. Plasmas* **9**, 2251 (2002).
38. J. A. Oertel *et al.*, *Rev. Sci. Instrum.* **70**, 803 (1999).
39. R. E. Olson *et al.*, *Bull. Am. Phys. Soc.* **47**, 329 (2002).
40. S. P. Marsh, ed. *LASL Shock Hugoniot Data*, Los Alamos Series on Dynamic Material Properties (University of California Press, Berkeley, CA, 1980).
41. C. E. Ragan III, *Phys. Rev. A* **25**, 3360 (1982).
42. W. J. Nellis *et al.*, *J. Appl. Phys.* **82**, 2225 (1997).
43. L. Suter *et al.*, *Phys. Plasmas* **7**, 2092 (2000).
44. L. Disdier *et al.*, *Nucl. Instrum. Methods Phys. Res. A* **489**, 496 (2002).